

# Squeezed and fragmented states of strongly interacting bosons in a double well

Joel C. Corbo,<sup>1,2,\*</sup> Jonathan L. DuBois,<sup>3</sup> and K. Birgitta Whaley<sup>1,4</sup>

<sup>1</sup>*Berkeley Center for Quantum Information and Computation,  
University of California, Berkeley, CA 94720, USA*

<sup>2</sup>*Department of Physics, University of California, Berkeley, CA 94720, USA*

<sup>3</sup>*Lawrence Livermore National Lab, 7000 East Ave, L-415, Livermore, CA 94550, USA*

<sup>4</sup>*Department of Chemistry, University of California, Berkeley, CA 94720, USA*

(Dated: July 19, 2015)

We present a systematic study of the phenomena of squeezing and fragmentation for a Bose-Einstein condensate (BEC) in a three dimensional double well potential over a range of interaction strengths and barrier heights. We compute the properties of the condensate both analytically, using a standard and an improved two-mode model and a recently-proposed eight-mode model, and numerically, through path integral ground state (PIGS) Quantum Monte Carlo simulations. We explicitly examine well geometries that exhibit appreciable overlap in the one-body wavefunctions localized in the left and right wells rather than assuming that they are nearly isolated from each other. We find that the truncated basis models agree with the numerically exact PIGS simulations for weak interactions, but fail to correctly predict the amount of squeezing and fragmentation exhibited by the PIGS simulations for strong interactions. Most significantly, we find that both squeezing and fragmentation show non-monotonic behavior with interaction strength. The Quantum Monte Carlo results are also found to show a universal scaling of squeezing with the product of number of atoms and interaction strength ( $Na$ ). We discuss the physical mechanisms that account for this behavior through a careful study of the ground state properties produced by various terms in the model Hamiltonians and the relationship between the strength of these terms and the system parameters defining the double well geometry and the atomic interaction strength.

PACS numbers: 67.85.Bc, 03.75.Hh

## I. INTRODUCTION

Since the achievement of Bose-Einstein condensation in the laboratory [1, 2], there has been significant experimental and theoretical interest in the study of a BEC in a double well trap. This system has been modeled extensively using several different theoretical approaches. One common approach is to use a variant of the Bose-Hubbard model within an  $n$ -mode approximation, in which the many-body state of the system is computed in terms of a basis constructed from the system's  $n$  lowest energy one-body states. The bulk of this work has been done in the context of a two-mode model [3–15]. although some authors have gone beyond two-mode models by including four [16] or eight modes [17]. Other authors have used multiconfigurational Hartree-Fock methods, in which a basis is constructed from a generalization of the two-mode basis using bosonic Hartree-Fock theory [18–21].

As discussed in [6], the two-mode model is generally restricted to the limit of weak particle interactions. Most studies focus on models which include only one-body tunneling ( $J$ ) and on-site interaction ( $U$ ) terms, although some include higher-order effects either through two-body tunneling terms [4, 11, 12] or renormalized  $J$  and  $U$  coefficients [13]. Recent theoretical work on un-

derstanding the double well in the context of an eight-mode approximation [17] has uncovered some deficiencies of the two-mode model. In particular, it was shown that even in regimes where one might naively expect only the lowest two single particle modes to contribute based on energy arguments, the ground state can nevertheless contain components of higher modes. Such admixtures have the potential to dramatically influence the collective properties of the system in ways that are not captured by including two-body effects into a two-mode model.

One such property is the degree of *number squeezing* exhibited by the system's many-body wavefunction. Number squeezing is related to the probability of finding particular values for the difference in the number of atoms on the two sides of the double well. In an unsqueezed system, the probabilities are distributed like a Gaussian centered on a difference of zero; in other words, while the most probable configuration is the one with an equal number of particles on each side of the barrier, there is non-negligible probability of finding other configurations. A system is said to be squeezed when this distribution narrows, so that the probability of observing a difference of zero dominates over all other possibilities. Broadly speaking, one can increase squeezing either by increasing the strength of the repulsive interparticle interaction (e.g., via a Feshbach resonance [22]) or by decreasing the tunneling strength between the wells (e.g., by increasing the barrier height).

Of the two-mode studies cited above, only [6, 7] explicitly considered squeezing, while this phenomenon has not yet been addressed within the eight-mode model or with

---

\* Email: joel.corbo@colorado.edu; Current affiliation: Center for STEM Learning, University of Colorado Boulder, Boulder, CO 80309

computational simulations. However, squeezing has implications for a number of important practical problems. One potentially powerful application is the development of methods for reducing the lower bound on the uncertainty of interferometric measurements from the standard quantum limit of  $N^{-1/2}$  to the Heisenberg limit of  $N^{-1}$  (where  $N$  is the total number of particles involved in the measurement) [23–25]. Proposals for doing so depend on the type of interferometry under consideration. For Sagnac-type interferometers, a cloud of BEC is split in two, and each resulting cloud travels a different path before they are recombined and their spatial interference pattern is observed. Initial proposals to reduce the quantum uncertainty in this system called for using superpositions of macroscopic quantum states (Schrödinger cat states), but sensitivity to dissipation was found to limit the benefits of this strategy [26]. However, the use of number squeezed states avoids this problem [27, 28]. Beginning in 2001, experimental efforts have succeeded in realizing number squeezed states with cold atoms in the laboratory [29–35].

In contrast, one can also perform interferometry on two different internal states of a quantum gas. In this situation, it is also possible to reduce the quantum uncertainty below the standard quantum limit via spin squeezing [36–39], which is conceptually similar to number squeezing and which has also been observed experimentally [40–43]. In this work, we focus our attention on number squeezing, since the double well system is particularly well-suited to Sagnac interferometry.

The symmetry of the double well potential also allows for *fragmentation* [44]. In a canonical BEC, we can express the system’s many-body wavefunction in such a way that all of the particles are in the same one-body state. Under the right conditions, the BEC can exhibit fragmentation, in which multiple one-body states are macroscopically occupied by the particles in the condensate. When population is further distributed over single-particle states with non-macroscopic occupation, the BEC is said to be *depleted*. Experimental studies have confirmed the presence of depletion in an atomic BEC in an optical lattice [45] as well as fragmentation in a quasi-1D atomic BEC in a magnetic waveguide [46]. Much theoretical effort has also gone into understanding fragmentation using two-mode models [47, 48], including studies of fragmentation in a double well [8–10]. As is the case with squeezing, these models are inadequate to fully capture the behavior of the system with respect to fragmentation at large interaction strengths. Indeed, studies that employed multiconfigurational Hartree-Fock methods have already demonstrated fragmentation behavior beyond that which is seen in traditional two-mode models [18, 19]; our results include similar behavior. Fragmentation and depletions have not yet been studied within the eight-mode model.

In this paper, we undertake a systematic study of the phenomena of squeezing and fragmentation for a repulsive Bose-Einstein condensate in a three dimensional dou-

ble well potential over a range of interaction strengths and barrier heights. We first conduct the analysis of these properties in the context of the two- and eight-mode models, extending the scope of these models as required. This analysis provides new information within the restricted domain of these models. In particular, unlike all previous finite mode calculations which assume no appreciable overlap between one-body wave functions localized in left and right wells (equivalently, near degeneracy of the lowest two modes), we explicitly examine well geometries that allow such overlap and show that this gives rise to a non-monotonic dependence of squeezing on interaction strength. Additionally, we employ the full many-body formalism of Quantum Monte Carlo (QMC) by evaluating the ground state properties of the BEC using the path integral ground state (PIGS) method [49–52]. The numerically exact PIGS method allows us to move beyond the range of validity of the  $n$ -mode models and into the regime of strongly interacting systems. We determine the amount of squeezing and fragmentation present in the BEC as a function of interaction strength and compare with the predictions of the two- and eight-mode models to understand when, how, and why these approximate models break down.

## II. THE SYSTEM

### A. The Many-Body Double Well Hamiltonian

The many-body Hamiltonian for  $N$  bosons of mass  $m$  interacting pairwise in an external potential has the form

$$\hat{H} = \sum_{j=1}^N \left( -\frac{\hbar^2}{2m} \nabla_j^2 + V_{ext}(\mathbf{r}_j) \right) + \sum_{j < k}^N V_{int}(\mathbf{r}_j, \mathbf{r}_k). \quad (1)$$

For the external potential, we use a three-dimensional double well potential of the form

$$V_{ext}(\mathbf{r}) = \frac{1}{2} m \omega_{ho}^2 \left( x^2 + y^2 + \alpha (z^2 - L^2)^2 \right), \quad (2)$$

where  $\omega_{ho}$  is the characteristic harmonic trap frequency in the  $xy$  plane,  $\alpha$  characterizes the height of the barrier between wells at  $z = 0$ , and  $2L$  is the distance between the minima of the wells (see Fig. 1). We present all of our results in terms of the system’s characteristic length  $a_{ho} = (\hbar/m\omega_{ho})^{1/2}$  and energy  $\hbar\omega_{ho}$ .

For  $\omega_{ho}$  and  $\alpha$  fixed, the parameter  $L$  can be used to scale the height of the potential barrier between the wells,  $V_{ext}(0) = \frac{1}{2} m \omega_{ho}^2 \alpha L^4$ . To analyze the behavior of squeezing and fragmentation over a wide range of potentials, we fix  $\alpha = 4/81 a_{ho}^{-2}$  and choose three different values of  $L$ ,  $L = a_{ho}$ ,  $2a_{ho}$ , and  $3a_{ho}$ , giving barrier heights  $2/81 \hbar\omega_{ho}$ ,  $32/81 \hbar\omega_{ho}$ , and  $2 \hbar\omega_{ho}$ , respectively, that range from very small to very high, as seen in Fig. 1. Table I lists the energies of the first four states of the double well for each of these three potentials, to give a sense

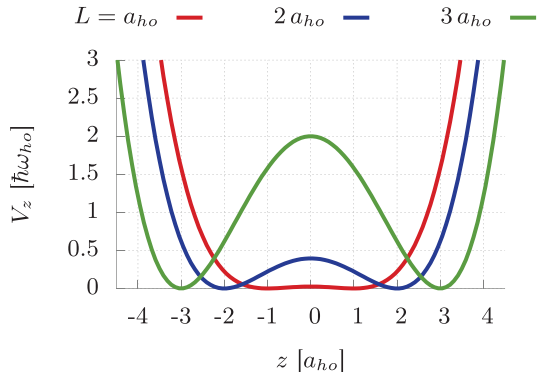


Figure 1. (Color online) The  $z$  component of the external potential for  $\alpha = 4/81 a_{ho}^{-2}$ . The height of the barrier,  $V_{ext}(0) = m\omega_{ho}^2 \alpha L^4 / 2$ , is  $2/81 \hbar\omega_{ho}$ ,  $32/81 \hbar\omega_{ho}$ , and  $2 \hbar\omega_{ho}$  for  $L = a_{ho}$ ,  $2a_{ho}$ , and  $3a_{ho}$ , respectively.

$L [a_{ho}]$	Energy [ $\hbar\omega_{ho}$ ]				
	$\phi_0(z)$	$\phi_1(z)$	$\phi_2(z)$	$\phi_3(z)$	$V_{ext}(0)$
1	0.167	0.594	1.220	1.946	0.025
2	0.297	0.482	1.026	1.614	0.395
3	0.634	0.637	1.681	1.801	2

Table I. Energies of the ground and first three excited states of the  $z$  component of the double well potential, as well as the energy of the double well barrier for  $\alpha = 4/81 a_{ho}^{-2}$  and three different potentials parameterized by  $L$  (see Sec. II A and Fig. 1). Note that these energies do not include the contribution from the  $x$  and  $y$  components of the state.

of where they lie relative to the height of the barrier. These states will be relevant to constructing models for the double well system in Sec. III.

We use the experiment described in [53] to give a realistic sense of the magnitude of the parameters of the external potential. This experiment used  $^{23}\text{Na}$  atoms and a trap with  $L = 6.5 \mu\text{m}$ ,  $\omega_{ho}/2\pi = 615 \text{Hz}$ , and  $\frac{1}{2}m\omega_{ho}^2 \alpha L^4 = h \times 4.7 \text{kHz}$  (equivalently,  $\alpha = 6.1 \times 10^{-9} \text{nm}^{-2}$ ). Thus,  $a_{ho} = 845 \text{nm}$  and  $\hbar\omega_{ho} = 2.54 \text{peV}$ , so  $L = 7.7 a_{ho}$  and  $\alpha = 0.26 a_{ho}^{-2}$ , which are comparable to the values in the systems we simulate.

We restrict our attention to BECs with repulsive interactions. Because we are interested in ground state (i.e., low energy) properties, we assume  $s$ -wave scattering and hence use a hard sphere interaction potential:

$$V_{int}(r_{jk}) = \begin{cases} \infty & r_{jk} \leq a \\ 0 & r_{jk} > a \end{cases}, \quad (3)$$

where  $r_{jk} = |\mathbf{r}_j - \mathbf{r}_k|$  and  $a$  is the positive  $s$ -wave scattering length, which determines the effective interaction strength. Substantial tunability of  $a$  has been demonstrated in the laboratory using Feshbach resonances. A particularly impressive example is [54], in which  $a$  for  $^7\text{Li}$  was tuned between  $0.53 \text{pm}$  and  $10.6 \mu\text{m}$  (between  $3.5 \times 10^{-7} a_{ho}$  and  $7 a_{ho}$ , given the value of  $\omega_{ho}$  above).

Our calculations employ values of  $a$  up to  $0.5 a_{ho}$  (about  $420 \text{nm}$ ), and are thus well within the range of experimental accessibility.

## B. The Differential Number Distribution and Squeezing

We are primarily interested in understanding the relationship between number squeezing and particle interaction strength. The differential number distribution is related to the operator  $\hat{n} = \frac{1}{2}(\hat{L} - \hat{R})$ , where  $\hat{L}$  is given in the position representation by

$$\hat{L} = \sum_{i=1}^N \begin{cases} 1 & z_i < 0 \\ 0 & z_i > 0 \end{cases}, \quad (4)$$

and  $\hat{R}$  is given by the analogous expression. For a completely symmetric state  $\Psi(\mathbf{r}_1, \dots, \mathbf{r}_N)$ , we find

$$\langle \Psi | \hat{L} | \Psi \rangle = N \int_{-\infty}^0 \left[ \int_{-\infty}^{\infty} \int_{-\infty}^{\infty} |\Psi_1(\mathbf{r}_1)|^2 dx_1 dy_1 \right] dz_1, \quad (5)$$

where

$$|\Psi_1(\mathbf{r}_1)|^2 = \int_{-\infty}^{\infty} \cdots \int_{-\infty}^{\infty} |\Psi(\mathbf{r}_1, \dots, \mathbf{r}_N)|^2 d\mathbf{r}_2 \cdots d\mathbf{r}_N, \quad (6)$$

and similarly for  $\langle \Psi | \hat{R} | \Psi \rangle$ . Intuitively,  $\hat{L}$  and  $\hat{R}$  measure the fraction of the probability density of the many-body state that exists in the left and right wells, respectively.

Because of the symmetry of the double well potential, the ground state of the system has  $\langle \Psi | \hat{L} | \Psi \rangle = \langle \Psi | \hat{R} | \Psi \rangle = N/2$  (and hence  $\langle \Psi | \hat{n} | \Psi \rangle = 0$ ) regardless of the strength of the interaction between the particles. However, the width of this distribution, characterized by its standard deviation  $\sigma_n = \sqrt{\langle \Psi | \hat{n}^2 | \Psi \rangle}$ , does vary with  $a$ . For the noninteracting ( $a = 0$ ) case, the many-body ground state consists of a product of single-particle ground states, and the particles are distributed according to a binomial distribution, with  $\sigma_n = \sqrt{N}/2$ . For a repulsive interaction ( $a > 0$ ), we expect that the number distribution will narrow because configurations with many particles on one side of the double well and few on the other will be energetically disfavored relative to configurations that more evenly split the particles between the two sides. This narrowing is what is meant by number squeezing. We define a squeezing parameter  $S$  to characterize the amount of squeezing in the system relative to the non-interacting ground state:

$$S = 1 - \frac{\sigma_n^2}{N/4} \\ = 1 - \frac{1}{N} \langle \Psi | (\hat{L} - \hat{R})^2 | \Psi \rangle. \quad (7)$$

$S = 0$  corresponds to no squeezing, and  $S = 1$  corresponds to a fully squeezed state, in which  $\sigma_n = 0$ .

Based on this qualitative argument, we would expect squeezing to increase with interaction strength. This is indeed the prediction of the two-mode mean-field model when the two wells are well-separated [6], but as we shall see below, it fails to hold when this condition is not met. The results of both the more accurate eight-mode model and the exact Quantum Monte Carlo simulations will also be shown to disagree with this simple picture.

### C. The One Body Density Matrix, Fragmentation, and Depletion

We analyze additional condensate properties by computing and diagonalizing the one body density matrix (OBDM), which constitutes a valid description of the BEC at all densities and interaction strengths [55, 56]. This computation results in the fraction of particles that are in the BEC and the state(s) they occupy, i.e., the extent of depletion and fragmentation, as a function of interaction strength, and provides another way to understand the breakdown of the mean-field models.

In a non-interacting system, the condensate is defined in terms of a single-particle ground state wavefunction, and the condensate fraction is the ratio of the number of particles occupying that state to the total number of particles. For a uniform system, momentum is a good quantum number, and the condensate is associated with the zero momentum state (this is true even when interactions are introduced, and the full many-body ground state may no longer be described by a single-particle wavefunction). In a finite, non-uniform, interacting system, neither of these prescriptions apply. Instead, analysis of the OBDM gives the condensate fraction and corresponding state in terms of the largest eigenvalue of the OBDM and its corresponding eigenvector [55, 57, 58].

The OBDM, which characterizes the correlations between the particle density at points  $\mathbf{r}$  and  $\mathbf{r}'$  in a many-body quantum state, is given by [57]

$$\rho(\mathbf{r}, \mathbf{r}') = \langle \hat{\Psi}^\dagger(\mathbf{r}) \hat{\Psi}(\mathbf{r}') \rangle, \quad (8)$$

where  $\hat{\Psi}(\mathbf{r})$  is the field operator that annihilates a single particle at the point  $\mathbf{r}$ .  $\hat{\Psi}(\mathbf{r})$  can be expanded in terms of a set of single-particle wavefunctions  $\phi_i(\mathbf{r})$  (the so called “natural orbitals”) and the corresponding annihilation operators  $\hat{a}_i$ :

$$\hat{\Psi}(\mathbf{r}) = \sum_i \phi_i(\mathbf{r}) \hat{a}_i. \quad (9)$$

At  $T = 0$ ,  $\rho(\mathbf{r}, \mathbf{r}')$  is evaluated with respect to the  $N$ -particle ground state wavefunction  $\Psi_0(\mathbf{r}_1, \dots, \mathbf{r}_N)$ , yield-

ing

$$\begin{aligned} \rho(\mathbf{r}, \mathbf{r}') &= \langle \Psi_0 | \hat{\Psi}^\dagger(\mathbf{r}) \hat{\Psi}(\mathbf{r}') | \Psi_0 \rangle \\ &= \sum_{ij} \phi_i^*(\mathbf{r}) \phi_j(\mathbf{r}') \langle \Psi_0 | \hat{a}_i^\dagger \hat{a}_j | \Psi_0 \rangle \\ &= \sum_i \phi_i^*(\mathbf{r}) \phi_i(\mathbf{r}') N_i \end{aligned} \quad (10)$$

where  $\sum_i N_i = N$ . The natural orbitals may thus be obtained as the eigenvectors of the OBDM in the position representation, and the corresponding eigenvalues  $N_i$  give the occupation numbers of these natural orbitals in the many-body ground state.

As a matter of notation, the natural orbital with highest occupation is given an index of 0, the next highest an index of 1, etc, and we denote the fraction of particles occupying a given natural orbital by  $n_i = N_i/N$ . Any natural orbital which is occupied in the thermodynamic limit (i.e., which has nonzero  $n_i$  as  $N$  approaches infinity) can be interpreted as a condensate. For a typical BEC, there is only one such natural orbital. When there is more than one, the BEC is *fragmented* [44]. In either case, the total small population distributed among the other natural orbitals that vanishes in the thermodynamic limit is known as the *depletion* [59]. Hence, fragmentation and depletion can be distinguished in principle because the occupation of individual depleted orbitals goes to zero in the thermodynamic limit, but the fragmented states maintain a finite occupation. In practice, however, all of our work is done at finite  $N$ , so the distinction between fragmentation and depletion is ambiguous. Below, we provide definitions for fragmentation and depletion parameters that are appropriate and useful for the double well system.

Intuitively, fragmentation in the double well can be related to the fluctuation of particles across the barrier. Suppose the barrier is very weak; then the ground state of the system is essentially the ground state of a single well, and there is no fragmentation. On the other hand, if the barrier is very strong, so that the wells can be thought of as isolated, then the particles in each well form independent condensates and the system is highly fragmented. Indeed, [8] predicted that the amount of fragmentation observed in a double well system would increase with the height of the barrier. Additionally, stronger interactions lead to reduced fluctuations, which constrains each atom in the system to occupy only one well. Thus, for strong repulsive interactions the condensate fragments into two independent condensates. This implies that fragmentation should also increase with interaction strength for a fixed barrier.

In analogy to the squeezing parameter  $S$ , we define fragmentation and depletion parameters,  $F$  and  $D$ . Reference [9] demonstrates that a condensate with  $G$ -fold degeneracy in its ground state can fragment into  $G$  parts, assuming low degeneracy ( $G \approx 1$ ). From the energies listed in Table I, we see that the single-particle ground state has near-degeneracy (i.e.,  $G \rightarrow 2$ ) when  $L$  becomes

large. Hence, it is reasonable to assume that, for the double well, at most two natural orbitals participate in fragmentation, and the rest, if occupied, constitute a very small amount of depletion (i.e.,  $n_0 + n_1 \approx 1$ ). This motivates the definition of fragmentation and depletion parameters ( $F$  and  $D$ ) as

$$F = 1 - |n_0 - n_1| \quad (11)$$

$$D = 1 - (n_0 + n_1). \quad (12)$$

With these definitions, a single condensate is represented by  $F \approx D \approx 0$  and a doubly fragmented condensate is represented by  $F \approx 1$  and  $D \approx 0$ . Because the OBDM in the two-mode model is a  $2 \times 2$  matrix, there are only two natural orbitals and two occupation numbers for the system within that context. Hence, the depletion as defined here is necessarily zero for a two-mode description (see Sec. III A 4) but can be non-zero for an eight-mode description and in the QMC simulations.

### III. TRUNCATED BASIS MODELS FOR AN INTERACTING BEC IN A DOUBLE WELL

Several simplified models have been proposed in attempts to reproduce the behavior of the interacting double well system while avoiding the difficulty of treating the interaction exactly. For comparison with the exact Quantum Monte Carlo calculations, we shall use two models that represent the Hamiltonian in a truncated basis of single particle states, specifically the oft-used two-mode model [3, 5–7, 11, 12] and a recently proposed eight-mode model [17].

The hard sphere interaction potential, Eq. (3), imposes the constraint that the wavefunction between two particles be 0 for  $r_{ij} \leq a$ . In the low energy limit and for  $r_{ij} \geq a$ , the wavefunction generated by the hard sphere potential is identical to the one that results from replacing this potential with a contact potential of the form [60, 61]

$$V_{int}(r_{jk}) = \frac{4\pi\hbar^2 a}{m} \delta(r_{jk}). \quad (13)$$

The Hamiltonian for the system is then

$$\hat{H} = \sum_{i=1}^N \left( \frac{\mathbf{p}_i^2}{2m} + V_{ext}(\mathbf{r}_i) \right) + \frac{4\pi\hbar^2 a}{m} \sum_{i<j} \delta(r_{jk}) \quad (14)$$

$$= \int d\mathbf{r} \hat{\Psi}^\dagger(\mathbf{r}) \left( -\frac{\hbar^2}{2m} \nabla^2 + V_{ext}(\mathbf{r}) \right) \hat{\Psi}(\mathbf{r}) + \frac{2\pi\hbar^2 a}{m} \int d\mathbf{r} \hat{\Psi}^\dagger(\mathbf{r}) \hat{\Psi}^\dagger(\mathbf{r}) \hat{\Psi}(\mathbf{r}) \hat{\Psi}(\mathbf{r}), \quad (15)$$

where

$$\hat{\Psi}(\mathbf{r}) = \sum_{i=1}^{\infty} \psi_i(\mathbf{r}) \hat{a}_i, \quad (16)$$

resulting in the second-quantized form

$$\hat{H} = \sum_{i,j=1}^{\infty} \hat{a}_i^\dagger \hat{a}_j \epsilon_{ij} + a \sum_{i,j,k,l=1}^{\infty} \hat{a}_i^\dagger \hat{a}_j^\dagger \hat{a}_k \hat{a}_l \kappa_{ijkl}, \quad (17)$$

with

$$\epsilon_{ij} = \int d\mathbf{r} \psi_i^*(\mathbf{r}) \left( -\frac{\hbar^2}{2m} \nabla^2 + V_{ext}(\mathbf{r}) \right) \psi_j(\mathbf{r}) \quad (18)$$

$$\kappa_{ijkl} = \frac{2\pi\hbar^2}{m} \int d\mathbf{r} \psi_i^*(\mathbf{r}) \psi_j^*(\mathbf{r}) \psi_k(\mathbf{r}) \psi_l(\mathbf{r}). \quad (19)$$

The (single-particle) energy of a state  $i$  is given by  $\epsilon_{ii}$ . For  $i \neq j$ , the  $\epsilon_{ij}$  parameters characterize the tunneling between states  $i$  and  $j$ . The  $\kappa_{ijkl}$  parameters characterize the strength of two-body interactions. Once the single-particle basis  $\psi_i(\mathbf{r})$  is specified, these parameters are then solely a function of the geometry of the potential.

In the following subsections, we describe the models obtained by expanding  $\hat{\Psi}(\mathbf{r})$  in a truncated basis of either two or eight single-particle (i.e., non-interacting) states. We have also considered constructing a basis out of states that are solutions to the Gross-Pitaevskii (GP) equation [11], with the goal of including the effects of interaction in the basis (i.e., these states are a function of  $N$  and  $a$ ). However, we found that in practice, the values of the  $\epsilon_{ij}$  and  $\kappa_{ijkl}$  coefficients do not depend strongly on this choice for the ranges of  $a$  and  $N$  studied here. In this situation, there is no real benefit to be gained from using GP solutions as a basis, while their dependence on  $a$  and  $N$  adds needless complexity to the calculations.

#### A. Two-mode model

The two-mode model includes the lowest two single-particle energy states of the 3D double well

$$\psi_{g/e}(\mathbf{r}) = \psi_0(x, y) \phi_{0/1}(z), \quad (20)$$

where  $\phi_0(z)$  and  $\phi_1(z)$  are the ground and first excited states, respectively, of the 1D double well and

$$\psi_0(x, y) = \psi_0^{ho}(x) \psi_0^{ho}(y), \quad (21)$$

is the ground state of a 2D harmonic oscillator. As is conventional, we expand  $\hat{\Psi}(\mathbf{r})$  in terms of linear combinations of these states that are localized in the left and right wells of the potential, i.e.,

$$\psi_{l/r}(\mathbf{r}) = \psi_0(x, y) \phi_{l/r}(z), \quad (22)$$

where

$$\phi_{l/r}(z) = \frac{1}{\sqrt{2}} (\phi_0(z) \pm \phi_1(z)), \quad (23)$$

with corresponding left and right annihilation (creation) operators  $a_l$  ( $a_l^\dagger$ ) and  $a_r$  ( $a_r^\dagger$ ), respectively. See Fig. 2 for examples of  $\phi_{0/1}(z)$  and  $\phi_{l/r}(z)$  for the three different potentials employed here.

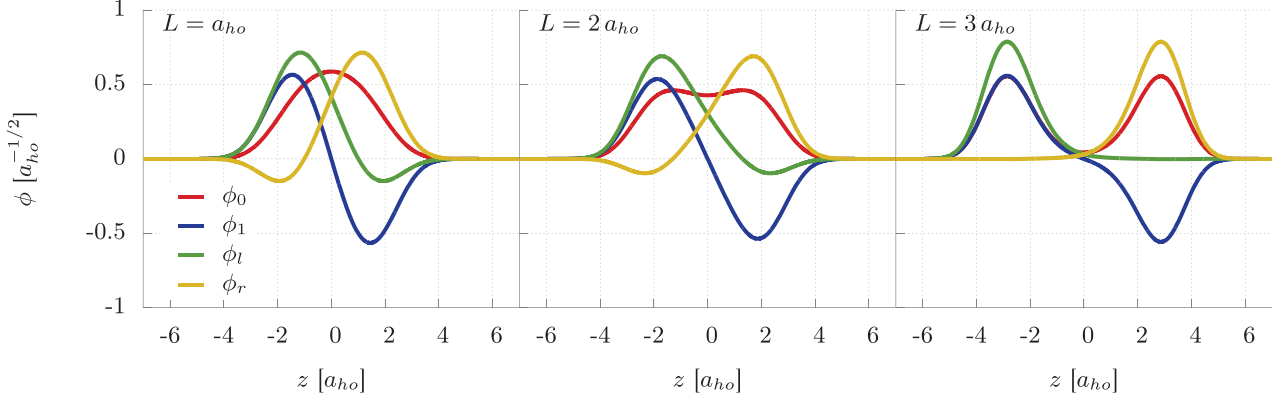


Figure 2. (Color online) The ground and first excited states of the  $z$  component of the double well potential ( $\phi_0$  and  $\phi_1$ ), and the left/right localized linear combinations of those states ( $\phi_l$  and  $\phi_r$ ) for  $\alpha = 4/81 a_{ho}^{-2}$  and  $L = a_{ho}, 2 a_{ho},$  and  $3 a_{ho}$ .

### 1. The two-mode Hamiltonian

By expanding  $\hat{\Psi}(\mathbf{r})$  in terms of Eq. (22), the Hamiltonian, Eq. (17), becomes

$$\begin{aligned} \hat{H} = & N(\Delta + a(N-1)\kappa_0)\hat{I} \\ & - 2a(\kappa_0 - 2\kappa_2)\hat{n}_l\hat{n}_r \\ & - (\delta/2 - 2a(N-1)\kappa_1)(\hat{a}_l^\dagger\hat{a}_r + \hat{a}_r^\dagger\hat{a}_l) \\ & + a\kappa_2(\hat{a}_l^\dagger\hat{a}_l^\dagger\hat{a}_r\hat{a}_r + \hat{a}_r^\dagger\hat{a}_r^\dagger\hat{a}_l\hat{a}_l), \end{aligned} \quad (24)$$

where  $\hat{n}_l$  ( $\hat{n}_r$ ) =  $a_l^\dagger a_l$  ( $a_r^\dagger a_r$ ),  $\delta = \epsilon_{ee} - \epsilon_{gg}$  (i.e., the energy difference between the excited and ground states),  $\Delta = (\epsilon_{ee} + \epsilon_{gg})/2$  (i.e., the average energy of the excited and ground states, or equivalently, the energy of the left and right localized states), and the  $\kappa$  parameters are shorthand for various combinations of the  $\kappa_{ijkl}$ 's. In particular,

$$\begin{aligned} \kappa_0 = \kappa_{llll} = \kappa_{rrrr} \\ = (\kappa_{gggg} + \kappa_{eeee} + 6\kappa_{ggee})/4 \end{aligned} \quad (25)$$

$$\begin{aligned} \kappa_1 = \kappa_{llrr} = \kappa_{lrrr} \\ = (\kappa_{gggg} - \kappa_{eeee})/4 \end{aligned} \quad (26)$$

$$\begin{aligned} \kappa_2 = \kappa_{llrr} \\ = (\kappa_{gggg} + \kappa_{eeee} - 2\kappa_{ggee})/4. \end{aligned} \quad (27)$$

Since the states are all real,  $\phi_0(z)$  is even,  $\phi_1(z)$  is odd, and  $\phi_l(z) = \phi_r(-z)$ , the parameters  $\kappa_i$  for  $i = 0, 1,$  and  $2$ , constitute the only distinct and nonzero matrix elements  $\kappa_{ijkl}$  in the two-mode model. Note that both  $\kappa_0$  and  $\kappa_2$  are positive, while  $\kappa_1$  can be positive or negative. We can estimate the relative size of these matrix elements by defining the function  $\beta(z)$ ,

$$\beta(z) = \phi_1^2(z) - \phi_0^2(z), \quad (28)$$

$L$ [ $a_{ho}$ ]	$\delta$ [ $\hbar\omega_{ho}$ ]	$\kappa$ [ $\hbar\omega_{ho}/a_{ho}$ ]		
		$\kappa_0$	$\kappa_1$	$\kappa_2$
1	$4.28 \times 10^{-1}$	$5.74 \times 10^{-2}$	$9.09 \times 10^{-4}$	$6.79 \times 10^{-3}$
2	$1.85 \times 10^{-1}$	$5.31 \times 10^{-2}$	$-1.22 \times 10^{-3}$	$2.85 \times 10^{-3}$
3	$3.02 \times 10^{-3}$	$6.93 \times 10^{-2}$	$-1.25 \times 10^{-4}$	$1.35 \times 10^{-6}$

Table II. Values of the energy splitting  $\delta$  and two-body interaction parameters  $\kappa_0$ ,  $\kappa_1$ , and  $\kappa_2$  for three trap geometries ( $L = a_{ho}, 2 a_{ho},$  and  $3 a_{ho}$ ).

from which

$$\begin{aligned} \kappa_0 = 2 \int_{-\infty}^{\infty} \phi_0^4(z) dz + 2 \int_{-\infty}^{\infty} \phi_0^2(z)\beta(z) dz \\ + \frac{1}{4} \int_{-\infty}^{\infty} \beta^2(z) dz \end{aligned} \quad (29)$$

$$\kappa_1 = -\frac{1}{2} \int_{-\infty}^{\infty} \phi_0^2(z)\beta(z) dz - \frac{1}{4} \int_{-\infty}^{\infty} \beta^2(z) dz \quad (30)$$

$$\kappa_2 = \frac{1}{4} \int_{-\infty}^{\infty} \beta^2(z) dz. \quad (31)$$

When  $\phi_0^2(z) \approx \phi_1^2(z)$  (i.e., the two modes are nearly degenerate, as in the case when  $L = 3 a_{ho}$ ),  $\beta(z) \ll 1$  and therefore  $\kappa_0 \gg |\kappa_1| \gg \kappa_2$ . Otherwise,  $\kappa_0 > |\kappa_1| \approx \kappa_2$ . See Table II for representative numerical values.

The natural basis for the two-mode Hamiltonian is a Fock basis  $|n\rangle$ , where  $|n\rangle$  consists of the fully-symmetrized state with  $n$  particles in the  $\psi_l(\mathbf{r})$  state and  $N-n$  particles in the  $\psi_r(\mathbf{r})$  state, i.e.,  $|n\rangle = |n\rangle_l |N-n\rangle_r$ . We can interpret the terms of the two-mode Hamiltonian, Eq. 24, in the context of this Fock basis as follows (where we have omitted the coefficients of the operators for brevity):

$\hat{I}$ : The energy that each Fock state has in common. We will ignore these terms when analyzing squeezing, because doing so does not alter the ground state wavefunction of the system.

$-\hat{n}_l\hat{n}_r$ : The state-dependent energy of each Fock state. This energy is lower the more evenly distributed the particles are, so  $|N/2\rangle$  is the ground state for this term when considered alone.

$-(\hat{a}_l^\dagger\hat{a}_r + \hat{a}_r^\dagger\hat{a}_l)$ : The energy due to transitions between Fock states that involve a single atom switching from the left to the right mode, or vice versa. This term depends on the scattering length  $a$ , in addition to the usual dependence on the energy gap  $\delta$  between the single-particle ground and excited states. The ground state for this part of the Hamiltonian alone is  $\frac{1}{2^{N/2}} \sum_{n=0}^N \sqrt{\binom{N}{n}} |n\rangle$ . Note that removing the minus sign in front of this term would leave the magnitude of the coefficients of this state unchanged but would cause their signs to alternate.

$\hat{a}_l^\dagger\hat{a}_l^\dagger\hat{a}_r\hat{a}_r + \hat{a}_r^\dagger\hat{a}_r^\dagger\hat{a}_l\hat{a}_l$ : The energy due to transitions between Fock states that involve exactly two atoms switching from the left to the right mode, or vice versa. This term is due entirely to interparticle interactions. A Hamiltonian which includes only these terms can be rewritten in a block-diagonal form with two blocks, where each block involves either the even-numbered or the odd-numbered Fock states. Hence, the ground state can only involve either even or odd Fock states, but not both. We can confirm this reasoning through an explicit computation of the ground state of this term alone, which shows it to be  $\frac{1}{2^{N/2}} \sum_{\substack{n=0 \\ n \in \text{even}}}^N \frac{\sqrt{n!(N-n)!}}{(n/2)!(N-n)/2!} |n\rangle$ .

## 2. Nearly degenerate two-mode model

Several previous studies [3, 5–7] have analyzed the double well system under the two-mode model with the assumption that the two modes are nearly degenerate, so that  $\phi_0^2(z) \approx \phi_1^2(z)$ . Physically, this can be achieved by imposing a high and/or wide barrier, i.e., large  $L$ . Mathematically, it amounts to assuming that  $\kappa_{gggg} = \kappa_{ggee} = \kappa_{eeee}$  (whence  $\kappa_1 = \kappa_2 = 0$ ), thereby reducing the two-mode Hamiltonian to

$$\hat{H} = -\frac{\delta}{2}(\hat{a}_l^\dagger\hat{a}_r + \hat{a}_r^\dagger\hat{a}_l) - 2a\kappa_0\hat{n}_l\hat{n}_r. \quad (32)$$

When the single-particle states lie below the barrier  $V_{ext}(0)$  (c.f. Table I), the first term describes single-particle tunneling between the left and right potential wells, quantified by the pure potential parameter  $\delta$  (note that the exact two-mode Hamiltonian of Eq. 24 has an additional  $a$ -,  $N$ -, and  $\kappa_1$ -dependent contribution to this amplitude).

This Hamiltonian has two natural limits. When tunneling dominates ( $a = 0$ ), the ground state is  $\frac{1}{2^{N/2}} \sum_{n=0}^N \sqrt{\binom{N}{n}} |n\rangle$  and there is no squeezing ( $S = 0$ ). When interactions dominate ( $\delta = 0$ ), the ground state is

$|N/2\rangle$  and squeezing is maximal ( $S = 1$ ). This behavior matches the qualitative argument made in Sec. II B.

Ref. [6] used the nearly degenerate two-mode model to compute an approximate analytical expression for the relative squeezing  $S$ . In the notation of the present work, this is given by

$$S_{nd2} = 1 - 2^{1/3} \begin{cases} \left( \frac{1}{2^{2/3} + Na/a^*} \right)^{1/2} & a \leq a^*N \\ N \left( \frac{a^*}{a} \right)^2 & a > a^*N \end{cases}, \quad (33)$$

where  $a^* = \delta/2^{10/3}\pi\kappa_0$  is a function of the geometry of the double well. As  $a$  ranges between zero and infinity, Eq. (33) predicts that  $S_{nd2}$  will vary monotonically between 0 and 1 (apart from a discontinuity of  $\mathcal{O}(N^{-3})$  at  $a = a^*N$  that is an artifact of the approximations entering the derivation of  $S_{nd2}$  [6]).

## 3. Exact two-mode model

The nearly degenerate two-mode model, while analytically tractable, misses many interesting features of the double well system that are also necessary to include for an informed comparison to the exact Quantum Monte Carlo calculations. To identify these features, we therefore analyze Eq. (24) without making the assumption of near-degeneracy between the single-particle ground and first excited states. We note that the full two-mode Hamiltonian was studied in [11] and the two-mode Hamiltonian with  $\kappa_2 = 0$  in [12], but neither included an analysis of squeezing, which is one of our primary goals.

The ground state of Eq. (24) is obtained via numerical diagonalization in the Fock representation using a restricted basis. Since the size of the Hilbert space is  $N+1$ , this diagonalization is tractable for  $N$  up to several thousand. Given the coefficients  $c_n$  from the expansion of the ground state (i.e.,  $|\psi_{gs}\rangle = \sum_{n=0}^N c_n |n\rangle$ ), the analytical expression for the two-mode squeezing  $S_2$  is

$$\begin{aligned} S_2 &= S_{max} \times \left( 1 - \frac{1}{N} \langle \psi_{gs} | (\hat{n}_l - \hat{n}_r)^2 | \psi_{gs} \rangle \right) \\ &= S_{max} \times \left( 1 - \frac{1}{N} \sum_{n=0}^N (N - 2n)^2 |c_n|^2 \right), \end{aligned} \quad (34)$$

with

$$S_{max} = \left( 1 - 2 \int_{-\infty}^{\infty} |\phi_l(z)|^2 dz \right)^2. \quad (35)$$

$S_{max}$  is the largest value of  $S_2$  achievable for a given potential and is achieved only in the pure  $|N/2\rangle$  state. For  $\alpha = 4/81 a_{ho}^{-2}$ , explicit evaluation of this expression yields values of  $S_{max} = 0.704, 0.820, \text{ and } 0.999$  for  $L = a_{ho}, 2a_{ho}, \text{ and } 3a_{ho}$ , respectively; as the barrier is increased,  $S_{max}$  increases to approach 1. The extent of squeezing in the exact two-mode model is therefore controlled by both

the value of  $S_{max}$ , which is determined solely by the well geometry, and the composition of the ground state (i.e., the  $c_i$  parameters), which is determined by both the well geometry and the interaction strength  $a$ .

For finite barriers,  $S_{max}$  is quite sensitive to the barrier height because it is a function of the degree of degeneracy of the two modes, which is controlled by the well geometry. When the modes are exactly degenerate, then all of the probability for  $\phi_l(z)$  is contained in the left well and  $S_{max} = 1$ . Otherwise, part of  $\phi_l(z)$  extends into the right side of the potential (and vice versa for  $\phi_r(z)$ ), and  $S_{max} < 1$ . Physically, this means that when the modes are not exactly degenerate, there is a nonzero probability of measuring a difference in the number of particles between the two wells, even in the  $|N/2\rangle$  state. Mathematically, this means that  $\hat{n}_l = \hat{L}$  and  $\hat{n}_r = \hat{R}$  only at complete degeneracy, so that  $S_2$  is then equivalent to  $S$  as defined in Eq. (7). One can thus interpret  $S_{max}$  as compensating for the fact that in the non-degenerate case (i.e., for realistic finite barrier heights), the operators in the two-mode Hamiltonian ( $\hat{n}_l$  and  $\hat{n}_r$ ) are not identical to the operators that define squeezing ( $\hat{L}$  and  $\hat{R}$ , see Eq. (4)).

An additional difference between the degenerate and non-degenerate cases is the dependence of the one- and two-particle tunneling amplitudes on  $a$  in Eq. 24 as compared with Eq. 32. In the degenerate case,  $|N/2\rangle$  is the ground state in the  $a \rightarrow \infty$  limit, but this is no longer true in the non-degenerate case. Indeed, the degeneracy of the system influences the composition of the ground state (and thus the amount of squeezing) for all nonzero values of  $a$ . The results presented in Sec. V A will show that for the exact two-mode model, not only is  $|N/2\rangle$  not the ground state in the  $a \rightarrow \infty$  limit, but also that squeezing does not necessarily increase monotonically as a function of  $a$ .

#### 4. Fragmentation and depletion in the two-mode model

We can also study fragmentation in the two-mode model by expanding the OBDM, Eq. (8), in terms of the left/right localized wave functions, Eqs. (22), and diagonalizing to find the occupation of the natural orbitals. This results in

$$\rho(\mathbf{r}, \mathbf{r}') = n_0 \phi_0(\mathbf{r}) \phi_0(\mathbf{r}') + n_1 \phi_1(\mathbf{r}) \phi_1(\mathbf{r}'), \quad (36)$$

where

$$n_{0/1} = \frac{1}{2} \pm \frac{1}{N} \sum_{n=0}^{N-1} \sqrt{(N-n)(n+1)} c_n c_{n+1}. \quad (37)$$

Thus, in the two-mode model, the natural orbitals are the single-particle ground and first excited states of the double well, and their occupations depend on the composition of the ground state of the system. The fragmentation and depletion parameters, Eqs. (12), are then given

by

$$F = 1 - \frac{2}{N} \left| \sum_{n=0}^{N-1} \sqrt{(N-n)(n+1)} c_n c_{n+1} \right| \quad (38a)$$

$$D = 0. \quad (38b)$$

The zero value of  $D$  is consistent with its definition (see Section II C). For the maximally-squeezed state  $|N/2\rangle$ ,  $F = 1$  and the system is maximally fragmented. For the noninteracting ground state, the sum evaluates to  $N/2$ , so that  $F = 0$  and there is no fragmentation. We note that there is no general one-to-one relationship between the squeezing parameter  $S$  and the fragmentation parameter  $F$  in the two-mode model.

## B. Eight-mode model

In an attempt to improve on the two-mode model, a recently-proposed eight-mode model [17] expands  $\hat{\Psi}(\mathbf{r})$  in terms of the two usual modes, Eqs. (22), and six additional modes. These additional modes may be constructed using left- and right-localized linear combinations of the second and third double well excited states,  $\phi_2(z)$  and  $\phi_3(z)$ :

$$\phi_{L/R}(z) = \frac{1}{\sqrt{2}} (\phi_2(z) \pm \phi_3(z)). \quad (39)$$

See Fig. 3 for examples of these states. Constructing additional two-dimensional harmonic oscillator states in the  $xy$ -plane,

$$\psi_{\pm}(x, y) = \frac{1}{\sqrt{2}} (\psi_0^{ho}(x) \psi_1^{ho}(y) \pm i \psi_1^{ho}(x) \psi_0^{ho}(y)), \quad (40)$$

allows the eight modes to be written as

$$\begin{aligned} \psi_{100}^{l/r}(\mathbf{r}) &= \psi_0(x, y) \phi_{l/r}(z) \\ \psi_{210}^{l/r}(\mathbf{r}) &= \psi_0(x, y) \phi_{L/R}(z) \\ \psi_{21\pm 1}^{l/r}(\mathbf{r}) &= \psi_{\pm}(x, y) \phi_{l/r}(z), \end{aligned} \quad (41)$$

where we have introduced a set of three subscripts to distinguish the modes. For a potential such that the curvature at the well minima is roughly equal in the  $x$ ,  $y$ , and  $z$  directions (as opposed to a pancake- or cigar-like geometry), the subscripts on  $\psi_{nlm}^{l/r}$  can be interpreted as the quantum numbers for a particle in a spherical potential [62]:  $n$  indexes the energy of the state and  $l$  and  $m$  its angular momentum magnitude and  $z$ -projection.

We note that since the relative energies of the single-particle states depend on the detailed three-dimensional geometry of the double well (i.e., on the parameters  $\omega_{ho}$ ,  $\alpha$ , and  $L$ ), then it is important that these parameters be chosen to ensure that the eight states, Eqs. (41), do have the lowest energies. The geometries used in the current work satisfy this property at the same time as

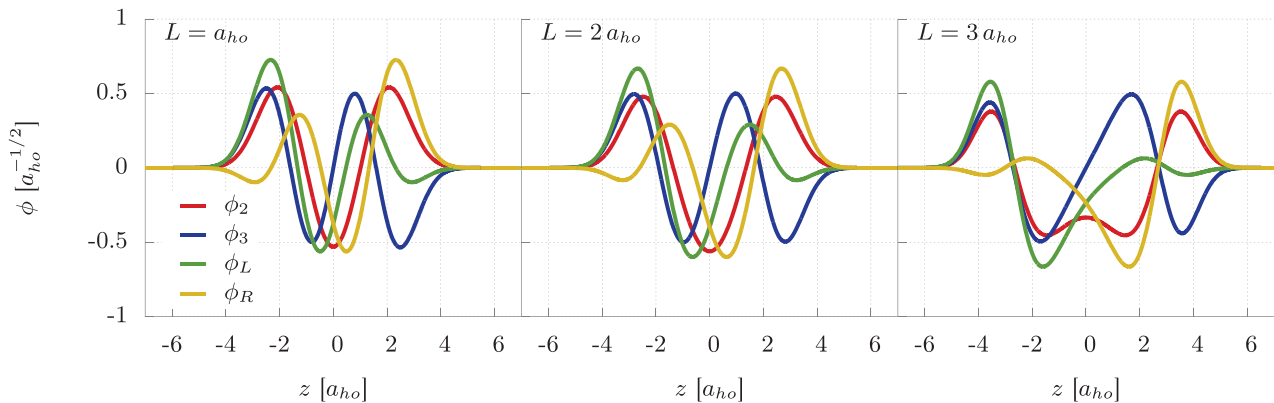


Figure 3. (Color online) The second and third excited states of the  $z$  component of the double well potential ( $\psi_2$  and  $\psi_3$ ), and the left/right localized linear combinations of those states ( $\psi_1^L$  and  $\psi_1^R$ ) for  $\alpha = 4/81 a_{ho}^{-2}$  and  $L = a_{ho}, 2 a_{ho},$  and  $3 a_{ho}$ , from left to right.

$L [a_{ho}]$	Energy [ $\hbar\omega_{ho}$ ]			
	100	21±1	210	$V_{ext}(0)$
1	1.38	2.38	2.58	0.025
2	1.39	2.39	2.32	0.395
3	1.64	2.64	2.74	2

Table III. Energies of the 8 modes and the double well barrier, for potentials with  $\alpha = 4/81 a_{ho}^{-2}$  and three different  $L$  values.

they illustrate the behavior of the system over a wide range of barrier strengths. Table III lists the energies of the modes for our three double well geometries.

As in the two-mode case, we use these eight modes to express the Hamiltonian in a Fock basis and diagonalize the resulting matrix, which we do not reproduce here. For  $N$  particles and  $M$  modes, the dimension of the Hilbert space is  $\frac{(N+M-1)!}{N!(M-1)!}$ , so the size of the matrix grows rapidly with  $N$  for  $M = 8$ . This restricts the practical usefulness of the eight-mode model to small  $N$  because of the computational cost of diagonalizing large matrices. However, the Hamiltonian has a block-diagonal form, with each block corresponding to a different value of  $m$  from  $-l$  to  $l$ . The ground state has  $m = 0$ , so one can make the diagonalization process easier by only diagonalizing the  $m = 0$  block. In this way, we were able to compute eight-mode model results for up to  $N = 10$ .

While one can in principle compute analytical expressions for the squeezing, fragmentation, and depletion parameters in the eight-mode model that are analogous to Eqs. (34), (38a), and (38b), the resulting expressions are not particularly illuminating. Instead, we analyze the differences in these properties between the two models with numerical calculations in Sec. V.

#### IV. THE PATH INTEGRAL GROUND STATE METHOD

We use the path integral ground state (PIGS) Quantum Monte Carlo method to make exact numerical calculations of the ground state properties of our system that go beyond the constraints of the two- and eight-mode models. PIGS is a many-body, ground state ( $T = 0$ ) method that uses imaginary time propagation and path sampling techniques to calculate the exact ground state expectation value for observables in a quantum system.

Conceptually, PIGS starts with a trial wave function that may be written as a sum over the energy eigenstates of the system:  $|\psi_T\rangle = \sum_{n=0}^{\infty} c_n |\psi_n\rangle$ . After applying the operator  $e^{-\tau\hat{H}}$ , normalizing, and taking the  $\tau \rightarrow \infty$  limit, the trial wave function decays into the ground state wave function:

$$\lim_{\tau \rightarrow \infty} \frac{e^{-\tau\hat{H}} |\psi_T\rangle}{\sqrt{\langle \psi_T | e^{-2\tau\hat{H}} | \psi_T \rangle}} = |\psi_0\rangle. \quad (42)$$

We will ignore the normalization factor for the rest of this discussion.

The configuration of the system is denoted by a  $3N$ -dimensional vector  $R$  that encodes the coordinates of the system's  $N$  particles:  $R \equiv \{\mathbf{r}_1, \mathbf{r}_2, \dots, \mathbf{r}_N\}$ . In the position representation, it is generally not possible to express  $\langle R | e^{-\tau\hat{H}} | R' \rangle$  analytically unless  $\tau$  is small. Therefore, we define  $\tau \equiv \beta M$ , with  $\beta \ll 1$ . The expectation value for an observable of interest  $\hat{A}$  (assumed to be diagonal in the position basis) can then be written as

$$\begin{aligned} \langle \hat{A} \rangle &= \langle \psi_T | (e^{-\beta\hat{H}})^M \hat{A} (e^{-\beta\hat{H}})^M | \psi_T \rangle \\ &= \int dR_0 \cdots dR_{2M} A(R_M) \psi_T^*(R_0) \psi_T(R_{2M}) \\ &\quad \times \prod_{i=0}^{2M-1} G(R_i, R_{i+1}, \beta), \end{aligned} \quad (43)$$

where we have inserted  $2M + 1$  complete sets of position eigenstates. Here,  $G(R_i, R_{i+1}, \beta) = \langle R_i | e^{-\beta \hat{H}} | R_{i+1} \rangle$  is the short time propagator, which may be approximated for sufficiently small  $\beta$ . This procedure can compute the expectation values of observables in the ground state, but not the ground state wave function itself.

Given an (exact or approximate) analytical form for  $G(R_i, R_{i+1}, \beta)$ , our problem has been transformed into that of solving an integral of very high dimension, which can be done with standard Monte Carlo sampling techniques. The paths  $X \equiv \{R_0, R_1, \dots, R_{2M}\}$  are statistically sampled from the probability density

$$\pi(X) = \psi_T^*(R_0) \psi_T(R_{2M}) \prod_{i=0}^{2M-1} G(R_i, R_{i+1}, \beta), \quad (44)$$

using the Metropolis algorithm [63], which ensures that the sampling is ergodic (i.e., that the set of accepted paths is a representative sample of the set of all paths). If this condition is met, then the average value of  $A(R_M)$  for the set of accepted paths can be used to estimate the value of  $\langle \hat{A} \rangle$ . In general, long paths (large  $M$ ) are required to ensure that  $R_M$  is sampled from a probability density as close to the square of the exact ground state wave function as possible.

The main computational difficulty faced when simulating interacting bosons in double well potentials is properly estimating the squeezing  $S$  for high barriers, because in this situation it is extremely difficult to achieve ergodicity with respect to moving particles across the barrier. Below we describe computational details regarding the trial function, the propagator, methods for path sampling, and the computation of off-diagonal observables, with explicit consideration of this issue.

### A. Trial function

We use a trial wave function which is a product of single-particle ground state wave functions and pair correlation (Jastrow) terms:

$$\psi_T(R) = \prod_{i=1}^N \psi_0(\mathbf{r}_i) \prod_{j < k}^N \left( 1 - \frac{a}{r_{jk}} \right), \quad (45)$$

where  $\psi_0(\mathbf{r}_i) = \psi_0^{HO}(x_i) \psi_0^{HO}(y_i) \psi_0^{DW}(z_i)$ , a product of the analytical harmonic oscillator ground state wave function in the  $x$  and  $y$  directions and a numerically calculated one-dimensional double well ground state wave function in the  $z$  direction. The pair correlation term is the exact zero-energy  $s$ -wave scattering solution for two hard spheres [58].

### B. Propagator

For our short-time propagator, we use a hybrid form that combines a fourth-order propagator decomposition

with a modification of the free particle propagator that exactly incorporates the hard sphere interaction.

#### 1. External potential decomposition

First, we use a fourth-order factorization to approximate  $G(R_i, R_{i+1}, \beta)$  [64]:

$$\begin{aligned} G(R_i, R_{i+1}, \beta) &= \int dR_j e^{-\frac{\beta}{6} V(R_i)} \langle R_i | e^{-\frac{\beta}{2}(T+V_{hs})} | R_j \rangle \\ &\quad \times e^{-\frac{2\beta}{3} \tilde{V}(R_j)} \langle R_j | e^{-\frac{\beta}{2}(T+V_{hs})} | R_{i+1} \rangle \\ &\quad \times e^{-\frac{\beta}{6} V(R_{i+1})}, \end{aligned} \quad (46)$$

where  $T$  is the kinetic energy,  $V$  is the external potential,  $V_{hs}$  is the hard-sphere potential,

$$\begin{aligned} \tilde{V} &= V + \frac{\tau^2}{48} [V, [(T + V_{hs}), V]] \\ &= V + \frac{\lambda \tau^2}{24} |\nabla V|^2, \end{aligned} \quad (47)$$

and  $\lambda = \frac{\hbar^2}{2m}$ . It is essential to group  $V_{hs}$  with  $T$  rather than  $V$  in the computation of  $\tilde{V}$ , in order to take advantage of the fact that  $[V, V_{hs}] = 0$  and thus avoiding the gradient of the (singular) hard sphere potential.

With this factorization we have introduced a new configuration  $R_j$  between each pair of original configurations  $R_i$  and  $R_{i+1}$ , so that there are now  $4M + 1$  configurations instead of  $2M + 1$ . Treating all of these on equal footing, we can rewrite Eq. (44) as

$$\begin{aligned} \pi(X) &= \psi_T^*(R_0) \psi_T(R_{4M}) e^{\frac{1}{6}\beta(V(R_0) - V(R_{4M}))} \\ &\quad \times \prod_{i=0}^{4M-1} f(R_i) G_{hs}(R_i, R_{i+1}, \beta/2), \end{aligned} \quad (48)$$

where

$$f(R_i) = \begin{cases} e^{-\frac{1}{3}\beta V(R_i)} & i = 0, 2, \dots \\ e^{-\frac{2}{3}\beta V(R_i) - \frac{1}{36}\lambda\beta^3 |\nabla V(R_i)|^2} & i = 1, 3, \dots \end{cases}, \quad (49)$$

and  $G_{hs}(R_i, R_{i+1}, \beta/2) = \langle R_i | e^{-\frac{\beta}{2}(T+V_{hs})} | R_{i+1} \rangle$  is the hard sphere propagator.

#### 2. Hard sphere propagator

To compute the hard sphere propagator, we use the pair product approximation [65]:

$$\begin{aligned} G_{hs}^m(R_i, R_{i+1}, \beta) &= G_{free}^m(R_i, R_{i+1}, \beta) \\ &\quad \times \prod_{j < k}^N \frac{G_{hs}^{m/2}(r_{jk}^i, r_{jk}^{i+1}, \beta)}{G_{free}^{m/2}(r_{jk}^i, r_{jk}^{i+1}, \beta)}. \end{aligned} \quad (50)$$

Here  $G_{free/hs}^{m/2}$  is the free/hard sphere propagator for the relative motion between two particles (a function of the relative coordinates  $r_{ij}$  and the reduced mass  $m/2$ ).

Several methods have been proposed in the literature for approximating  $G_{hs}$ , including the image approximation [65, 66] and the propagator of Cao and Berne [67]. One critical consideration for choosing a propagator for the double well system is that we need long paths to ensure that the system has decayed to the ground state because the decay goes as  $\exp(-\tau\Delta E)$ , where  $\Delta E$  (the energy gap between the ground and first excited state) is small. Hence, we must use as large a time step as possible. We therefore implement the exact hard sphere propagator here, because it allows larger time steps than the Cao and Berne propagator (e.g.,  $10^{-2}(\hbar\omega_{ho})^{-1}$  compared to  $10^{-4}(\hbar\omega_{ho})^{-1}$  for equivalent results).

The exact expression for  $G_{hs}^{m/2}$  is the non-closed form [68]:

$$G_{hs}^{m/2} = \frac{1}{2\pi^2} \sum_{l=0}^{\infty} P_l(\cos \gamma)(2l+1) \times \int_0^{\infty} k^2 e^{-2\beta\lambda k^2} \frac{R_l(r_{jk}^i, k) R_l(r_{jk}^{i+1}, k)}{D_l(k)} dk, \quad (51)$$

where

$$R_l(r, k) = j_l(kr)y_l(ka) - y_l(kr)j_l(ka), \quad (52)$$

$$D_l(k) = j_l^2(ka) + y_l^2(ka), \quad (53)$$

$j_l(x)$  and  $y_l(x)$  are spherical Bessel functions, and  $\gamma$  is the angle between  $r_{jk}^i$  and  $r_{jk}^{i+1}$ . To use this expression for  $G_{hs}^{m/2}$ , we must terminate the sum at some appropriate  $l_{max}$  and tabulate it as a function of  $r_{jk}^i$ ,  $r_{jk}^{i+1}$ , and  $\gamma$ .

An efficient computational representation of Eq. (50) may be achieved by rewriting the conventional closed form of  $G_{free}^{m/2}$

$$G_{free}^{m/2} = \frac{1}{(8\pi\beta\lambda)^{3/2}} e^{-\frac{(r_{jk}^i - r_{jk}^{i+1})^2}{8\beta\lambda}}, \quad (54)$$

as a summation similar to Eq. (51), namely,

$$G_{free}^{m/2} = \frac{1}{2\pi^2} \sum_{l=0}^{\infty} P_l(\cos \gamma)(2l+1) \times \int_0^{\infty} k^2 e^{-2\beta\lambda k^2} j_l(kr_{jk}^i) j_l(kr_{jk}^{i+1}) dk. \quad (55)$$

The *difference* between  $G_{hs}^{m/2}$  and  $G_{free}^{m/2}$  converges with respect to  $l_{max}$  much faster than  $G_{hs}^{m/2}$  alone. We can use this fact to reexpress the quotient in the pair product

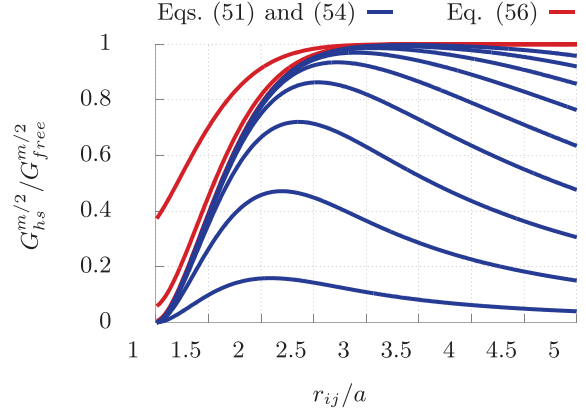


Figure 4. (Color online) Comparison of convergence with respect to  $l_{max}$  of the ratio  $G_{hs}^{m/2}/G_{free}^{m/2}$  computed using conventional expressions (Eqs. (51) and (54), blue curves) versus using the difference expression (Eq. (56), red curves), for  $r_{jk}^i = r_{jk}^{i+1}$ ,  $\gamma = 0$ , and  $a^2 = 2\beta\lambda$ . Both sets of curves are computed for integer values of  $l_{max}$  from 0 to 8; the  $l_{max} = 0$  curve is the highest (lowest) curve in the red (blue) set. The red curves with  $l_{max}$  between 2 and 8 are visually indistinguishable. The more rapid convergence of this ratio when computed using the difference expressions compared with the conventional expressions is a general feature of these functions.

approximation:

$$\begin{aligned} \frac{G_{hs}^{m/2}}{G_{free}^{m/2}} &= 1 - \frac{G_{free}^{m/2} - G_{hs}^{m/2}}{G_{free}^{m/2}} \\ &= 1 - \frac{4(2\beta\lambda)^{3/2}}{\pi^{1/2}} e^{-\frac{(r_{jk}^i - r_{jk}^{i+1})^2}{8\beta\lambda}} \\ &\quad \times \sum_{l=0}^{\infty} P_l(\cos \gamma)(2l+1) \\ &\quad \times \int_0^{\infty} k^2 e^{-2\beta\lambda k^2} A_l(k, r_{jk}^i, r_{jk}^{i+1}) dk, \quad (56) \end{aligned}$$

where

$$A_l(k, r, r') = j_l(kr)j_l(kr') - \frac{R_l(r, k)R_l(r', k)}{D_l(k)}. \quad (57)$$

By using this alternative form for the ratio in Eq. (50), we can terminate the sum at a value of  $l_{max}$  about 2 to 10 times smaller (depending on the value of  $a$ ) than would be necessary to achieve the same precision using Eq. (51). This is demonstrated explicitly in Fig. 4.

### C. Sampling methods

For simulations with a double well trapping potential, the key sampling issue is achieving ergodicity with respect to the motion of particles between the two wells. In general, paths which are entirely located in one well

are more probable than paths that cross the barrier, because of the extra potential energy associated with the parts of the paths that are in the barrier region. The larger this difference in probability, the less likely it will be that paths that start in one well will move to the other over the course of the simulation. Instead, the paths are often stuck on one side. This problem becomes worse for larger barriers, and is also exacerbated for small  $N$  and small  $a$ , which one can intuitively understand as follows. The number of paths is given by  $N$ , and the minimum distance between different paths at the same time slice is given by  $a$ . When both of these are small, paths can “settle down” into the bottoms of the wells where the potential energy is low. However, when either  $N$  or  $a$  are large, the paths are forced to spread out into regions where the potential is larger, which makes it easier for them to transition through the barrier because the “probability penalty” incurred is not as great.

This ergodicity problem impacts the computation of  $S$  more severely than other observables such as the energy or density. Since  $S$  is a function of  $(n_l - n_r)^2$ , which only changes value when the center of a path crosses the barrier at  $z = 0$ , reduced ergodicity with respect to particle motion across the barrier leads to long autocorrelation times for  $S$ . Hence, one must wait an unusually long time before the simulation generates enough independent values of  $(n_l - n_r)^2$  to compute precise values of the squeezing  $S$ .

Here we describe sampling methods that mitigate this problem in certain circumstances.

### 1. Brownian Bridge Moves

The main “workhorse” update method we use is the Brownian bridge move, which is a specific realization of the more general Lévy construction [69, 70]. In the Brownian bridge move, a portion of the path of a single particle is updated. The particle is chosen randomly, as is the section of its path that is updated; the length of this section is a fixed parameter  $K$ , defined such that the section consists of  $K + 1$  time slices, including the endpoints.

The move proceeds as follows. The endpoints of the section to be updated are chosen and held fixed; call these  $\mathbf{r}_0$  and  $\mathbf{r}_K$ . Next, the coordinate of the particle at the first time slice,  $\mathbf{r}_1$ , is replaced with one drawn from the probability distribution

$$P(\mathbf{r}_1) \propto e^{-\frac{\hbar(\mathbf{r}_1 - \mathbf{r}^*)^2}{4\lambda\tau^*}}, \quad (58)$$

where

$$\mathbf{r}^* = \frac{\tau_1 \mathbf{r}_0 + \tau_2 \mathbf{r}_K}{\tau_1 + \tau_2} \quad (59a)$$

$$\tau^* = \frac{\tau_1 \tau_2}{\tau_1 + \tau_2}. \quad (59b)$$

Here,  $\tau_1$  is the amount of imaginary time separating  $\mathbf{r}_0$  and  $\mathbf{r}_1$  and  $\tau_2$  is the amount of imaginary time separating  $\mathbf{r}_1$  and  $\mathbf{r}_K$ . This coordinate becomes the new left

endpoint for a section of length  $K - 1$  that runs from  $\mathbf{r}_1$  to  $\mathbf{r}_K$ . The coordinate of the particle at the second time slice,  $\mathbf{r}_2$ , is replaced with one drawn using a probability distribution with the same form as the one used for determining  $\mathbf{r}_1$ , but with the updated left endpoint. This process continues until the entire section of path is reconstructed.

In general, the Brownian bridge move is an efficient way of sampling new paths, although it is susceptible to the ergodicity problem described above if the barrier is too strong and enough of the new path ends up in the barrier region. For the vast majority of our simulations, however, it was the only update method that was necessary.

### 2. Swap moves

One potential way to address the ergodicity issue is to implement an additional type of move that explicitly transfers a particle from one well to the other [71]. In our implementation of this “swap move,” the  $z$ -coordinate is negated for the entire path of a random particle. If this leads to an overlap between the swapped path and another path (i.e., two particles at the same time slice with a separation less than  $a$ ), then the other path is also swapped. This “cascade” continues until no overlaps remain.

Unfortunately, swap moves do not work as well as intended. As the simulation progresses, Brownian bridge moves tend to nudge the particle paths into tight clusters near the well minima, as noted above. Once the system is in that sort of configuration, a swap move has a high probability of leading to a cascade that swaps every particle, which is equivalent to not swapping any particle. This effect is worse for longer paths and larger  $N$ , and in practice, the swap move was found to be mostly ineffective for the double well simulations described here.

### 3. Potential moves

Our “potential moves” were inspired by the parallel tempering technique [72]. In parallel tempering, one runs multiple copies of a simulation at different temperatures simultaneously, and exchanges configurations between two different simulations based on the Metropolis criterion. This allows a simulation at a given temperature to sample a wider variety of configurations, potentially avoiding an ergodicity problem.

In our potential moves, we run only one simulation, but we implement a move that changes the shape of the external potential, specifically by changing  $L$  from among a set of pre-defined values. Given the current value of  $L$ , the potential move attempts to change  $L$  to the next highest or lowest value in the pre-defined set and uses the Metropolis criterion to accept or reject the move. The motivation here is to allow for a way to more easily

N	Number of slices		
	100	200	800
8	$4.8 \times 10^{-1}$	$3.9 \times 10^{-1}$	$6.1 \times 10^{-2}$
16	$3.0 \times 10^{-1}$	$1.5 \times 10^{-1}$	$1.8 \times 10^{-2}$
32	$1.2 \times 10^{-1}$	$4.6 \times 10^{-2}$	$1.0 \times 10^{-5}$
64	$4.8 \times 10^{-2}$	$1.1 \times 10^{-2}$	$3.1 \times 10^{-12}$

Table IV. Probability of making a “potential move” that transitions between two potentials of different shape, characterized by  $L = 2.875 a_{ho}$  and  $3 a_{ho}$ , for various numbers of particles  $N$  and path lengths (number of slices). In all cases,  $a = 0.1 a_{ho}$ .

change  $(n_l - n_r)^2$  for a high-barrier potential than would be possible with only Brownian bridge moves: lower the potential barrier and then raise it again.

One challenge with this method is that certain potentials are more probable than others (i.e., they have higher average values of  $\pi(X)$ , where the average is taken over all configurations), so a simulation with potential moves as described above would eventually end up only sampling the most probable potential. To avoid this problem, we introduce a set of weights, one per potential, that we multiply by  $\pi(x)$  before applying the Metropolis algorithm. We choose these weights so that the average probability of transitioning from one potential to another is the same as the probability of the reverse, which ensures that all of the potentials will be visited with equal probability in the long run. One can choose these weights using a version of the Wang and Landau algorithm [73].

In practice, these moves often work quite well once the correct weights are chosen. However, there is still a problem: while weights can be chosen to equalize the back-and-forth transition probabilities between two potentials, the actual *value* of that probability cannot be tuned at will and can be quite small. If that is the case, then even though in principle all potentials will be visited with equal frequency, that will only happen in practice in the limit of a very long simulation. This situation arises for high-barrier potentials, and worsens for larger  $N$  and longer paths; see Table IV for an example.

#### D. Off-diagonal observables

The presentation of PIGS above describes the calculation of observables diagonal in the position basis. To compute an off-diagonal observable, such as the OBDM, we insert an extra set of position eigenstates into Eq. (43) at  $R_{M+1}$ :

$$\begin{aligned} \langle \hat{A} \rangle &= \int dR_0 \cdots dR_{2M+1} A(R_M, R_{M+1}) \psi_T^*(R_0) \psi_T(R_{2M}) \\ &\times \prod_{i=0}^{M-1} G(R_i, R_{i+1}, \beta) \prod_{i=M+1}^{2M} G(R_i, R_{i+1}, \beta). \end{aligned} \quad (60)$$

There is no propagator connecting the configurations  $M$  and  $M+1$ ; the path is said to be “broken.” The paths are sampled in the same way as for diagonal observables, and the value of the off-diagonal operator  $\langle \hat{A} \rangle$  is estimated by averaging over  $A(R_M, R_{M+1})$  for the accepted paths, just as before.

To compute the OBDM [50], the path of only one of the  $N$  particles is broken (i.e.,  $\mathbf{r}_M$  is allowed to differ from  $\mathbf{r}_{M+1}$  for the broken path) while  $\mathbf{r}_M$  is set equal to  $\mathbf{r}_{M+1}$  for the others. One then samples paths as usual and uses the set of accepted configurations to make a histogram of the occurrences of particular pairs of  $z_M$  and  $z_{M+1}$  for the *broken* path; this histogram is  $\rho(z, z')$ . In order to normalize the OBDM, we multiply it by a factor such that the sum of its eigenvalues (i.e., the total occupation of the natural orbitals) is 1. Note that because of the finite bin sizes, this method can artificially generate non-physical negative eigenvalues for small sampling, but these vanish given long enough simulations.

## V. RESULTS & DISCUSSION

We now present the numerically exact PIGS results for squeezing and fragmentation of a BEC in a three-dimensional double well potential, with a critical comparison to the corresponding results from the two- and eight-mode approximations. We show results for the three double well potentials with parameters  $\alpha = 4/81 a_{ho}^{-2}$  and  $L = a_{ho}, 2 a_{ho},$  and  $3 a_{ho}$ . As discussed above, these particular potentials are chosen to allow study of a range of barrier heights while staying in a regime where it is sensible to apply both the two-mode and eight-mode models.

### A. Two-mode model results

We first present the nearly-degenerate and exact two-mode model results for squeezing and fragmentation.

#### 1. Squeezing

Fig. 5 shows the behavior of  $S$  as a function of  $a$  for a variety of particle numbers and in three different double well geometries, for both the nearly degenerate and the exact two-mode models. It is evident that the models agree well only for small values of  $a$ , with deviations between them growing as  $N$  increases. There are several notable features of the results in Fig. 5 not seen in previous studies. These are the lack of monotonicity (especially for low barriers) for  $S$  vs.  $a$ , the tendency of  $S$  to increase as the extent of mode degeneracy increases (i.e., for higher barriers), and the tendency of  $S$  to decrease as a function of  $N$  for large  $a$ .

The degree of squeezing  $S$  is of course a reflection of the composition of the ground state. In Fig. 6, this composition is represented by plotting  $|c_n|^2 = |\langle n | \psi_{ground} \rangle|^2$

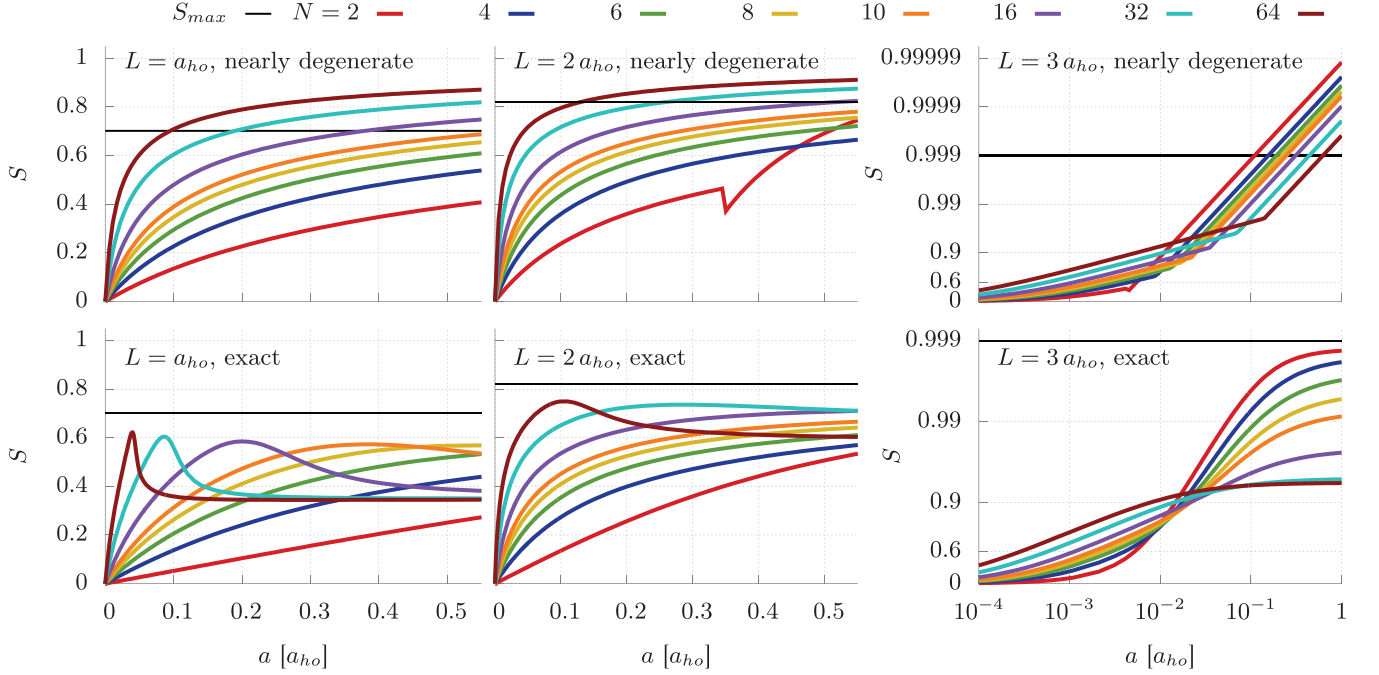


Figure 5. (Color online) Squeezing  $S$  vs. scattering length  $a$  for values of the particle number  $N$  between 2 and 64, for three different potentials ( $L = a_{ho}$ ,  $2 a_{ho}$ , and  $3 a_{ho}$  from left to right). The upper and lower plots are of  $S$  as computed in the nearly degenerate two-mode model (Eq. (33)) and the exact two-mode model (Eq. (34)), respectively. All plots also indicate the value of  $S_{max}$  from Eq. (35).

as a function of  $a$ . The squeezing analysis in Sec. II B would suggest that each of these plots should show a smooth transition from a binomial distribution centered at  $n = N/2$  to sole occupancy of the  $n = N/2$  state as  $a$  increases from 0. This is clearly not what happens for  $N = 64$  particles. For  $L = a_{ho}$ , the ground state settles into a very wide “striped” pattern, with occupancy of every other Fock state, for  $L = 2 a_{ho}$  it settles into a different striped pattern, and for  $L = 3 a_{ho}$  it settles into a narrow but wider-than-one-state distribution. Even for 8 particles, the distribution narrows to the state  $|4\rangle$  only for the highest barrier,  $L = 3$ , and the largest  $a$  values,  $a \geq 0.1$ . Based on the definition of  $S_2$ , Eq. (34), the width or “spread” of these patterns gives a qualitative sense of the degree of squeezing: narrower means more squeezing and vice versa. We can thereby see that the progression of these patterns is consistent with the trends seen in the squeezing plots displayed in Fig. 5.

Ideally, one could simply use the expression for  $S$  in Eq. (34) to explain the observed trends. For example, the form of  $S_{max}$  implies that, in general, one should expect more squeezing for potentials with a higher degree of degeneracy between the two modes; this is supported by the data. However, there is no explicit analytical expression for the coefficients  $c_n$  for the exact two-mode Hamiltonian that allows the dependence of  $S_2$  on  $a$  and  $L$  to be extracted.

We therefore study the ground state in different parameter regimes. In previous work, the nearly-degenerate

two-mode Hamiltonian, Eq. (32), has been described in terms of three regimes: Rabi, Josephson, and Fock (see, e.g., [56]). The Rabi regime is the one in which the two-body interactions are negligible compared with the effects of single-particle tunneling, whereas in the other two regimes the two-body interactions dominate. The Josephson and Fock regimes are further distinguished in that the interactions are so strong in the Fock regime that number fluctuations are suppressed (i.e., the ground state is  $|N/2\rangle$ ) while in the Josephson regime there are still some fluctuations due to one-particle tunneling. These regimes are defined by the value of the dimensionless parameter  $\chi = 4a\kappa_0/\delta$ . The Rabi regime has  $\chi \ll N^{-1}$ , the Josephson regime has  $N^{-1} \ll \chi \ll N$ , and the Fock regime has  $N \ll \chi$ .

To make contact between these different regimes for the nearly-degenerate two mode model and the behavior of the exact two-mode system, we rewrite the full two-mode Hamiltonian as

$$\hat{H} = -(\hat{a}_l^\dagger \hat{a}_r + \hat{a}_r^\dagger \hat{a}_l) + \chi_1(a, N) \hat{H}', \quad (61)$$

where

$$\hat{H}' = -\hat{n}_l \hat{n}_r + \chi_2(\hat{a}_l^\dagger \hat{a}_l^\dagger \hat{a}_r \hat{a}_r + \hat{a}_r^\dagger \hat{a}_r^\dagger \hat{a}_l \hat{a}_l), \quad (62)$$

$$\chi_1(a, N) = \frac{a\chi_1^*}{a^* - a(N-1)}, \quad (63)$$

$$\chi_2 = \frac{\kappa_2}{2(\kappa_0 - 2\kappa_2)}, \quad (64)$$

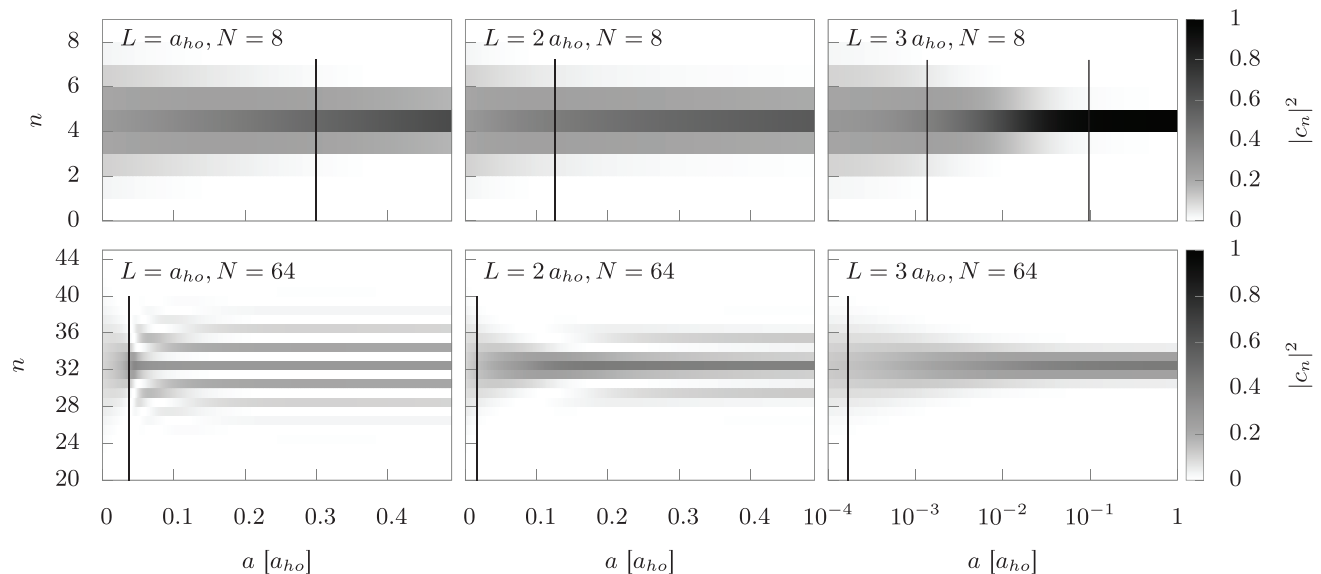


Figure 6. The components of the ground state  $|c_n|^2 = |\langle n | \psi_{ground} \rangle|^2$  for the double well potential as a function of scattering length  $a$ , as computed in the exact two-mode model (Eqs. (61)–(64)) for  $N = 8$  (top row) and  $64$  (bottom row) for  $L = a_{ho}$ ,  $2a_{ho}$ , and  $3a_{ho}$  (left to right). The vertical lines indicate the boundaries between the Rabi-, Josephson-, and Fock-like regions, from left to right in each plot (although only the  $L = 3a_{ho}$ ,  $N = 8$  plot has a Fock-like regime visible). In addition to the indicated regimes, the  $L = a_{ho}$ ,  $N = 8$  plot has a Fock-like regime between  $a = 9.03$  and  $121$  (and a Josephson-like regime thereafter) and the  $L = a_{ho}$ ,  $N = 64$  plot has a Fock-like regime between  $a = 1.85$  and  $1.98$  (and a Josephson-like regime thereafter).

$L$ [ $a_{ho}$ ]	$a^*$ [ $a_{ho}$ ]	$\chi_1^*$	$\chi_2$
1	117.6	48.2	$7.74 \times 10^{-2}$
2	-37.9	-38.8	$3.01 \times 10^{-2}$
3	-6.0	-553.2	$9.73 \times 10^{-6}$

Table V. Values of  $a^*$ ,  $\chi_1^*$ , and  $\chi_2$  for  $L = a_{ho}$ ,  $2a_{ho}$ , and  $3a_{ho}$ .

and we have defined  $a^* = \delta/4\kappa_1$  and  $\chi_1^* = (\kappa_0 - 2\kappa_2)/\kappa_1$ , both of which are functions solely of the geometry of the double well. We analyze this Hamiltonian in two stages. First, we study the effect on the ground state of variations in  $\chi_1$ ; for small  $\chi_1$ , the Hamiltonian is dominated by one-body tunneling whereas for large  $\chi_1$  it is dominated by  $\hat{H}'$ . Then, we study the effects of variations in  $\chi_2$  on the ground state of  $\hat{H}'$  alone (Fig. 9). Finally, we combine these together to understand the variation of both  $\chi_1$  and  $\chi_2$  on the ground state of the full Hamiltonian Eq. 61 (Fig. 10). For the geometries studied in this work,  $\kappa_0 - 2\kappa_2 > 0$  (see Table II), so the signs of  $a^*$  and  $\chi_1^*$  are the same as the sign of  $\kappa_1$ . See Table V for representative numerical values for these parameters.

Because  $\chi_1$  reduces to  $\chi$  when  $\kappa_1 = \kappa_2 = 0$ , the Hamiltonian of Eq. (61) reduces to Eq. (32) in the nearly degenerate limit, as it should. This motivates us to generalize the definitions of the three two-mode regimes that have been defined previously for the nearly-degenerate two-mode model, to the full two-mode system. As an ex-

ample, recall that physically the Rabi regime is the one in which two-body interactions are negligible. Because  $\chi_1$  can be both positive or negative, this physical condition corresponds mathematically to both  $0 < \chi_1 \ll N^{-1}$  and  $0 > \chi_1 \gg -N^{-1}$  (equivalently,  $|\chi_1| \ll N^{-1}$ ) in Eq. (61). Hence, we define a Rabi-like regime as  $|\chi_1| \ll N^{-1}$ . Similarly, we define a Josephson-like regime as  $N^{-1} \ll |\chi_1| \ll N$  and a Fock-like regime as  $N \ll |\chi_1|$ .

In Fig. 7 we schematically plot  $|\chi_1|$  as a function of  $a$  for both positive and negative  $\kappa_1$ . For positive  $\kappa_1$ , we see that the system will have Rabi-, Josephson-, and Fock-like regimes for some range of interaction strength  $a$ , since  $|\chi_1|$  diverges at  $a = a^*/(N-1)$ . For negative  $\kappa_1$ , the system will have a Rabi-like regime but may or may not have Josephson- or Fock-like regimes, depending on whether  $|\chi_1^*| < N^{-1}$ ,  $N^{-1} < |\chi_1^*| < N$ , or  $N < |\chi_1^*|$ . In Fig. 8, we plot  $|\chi_1|$  as a function of  $a$  for the same six sets of parameters that are depicted in Fig. 6; we also include the values of  $N$  and  $N^{-1}$  in the plots to make it clear where transitions between the three regimes occur. These transitions correspond to the vertical lines in Fig. 6 (see also the description in the caption to Fig. 6).

In the case where  $\chi_1$  is large (and the Hamiltonian is dominated by  $\hat{H}'$ ), the ground state also depends on the value of  $\chi_2$ . In Fig. 9, we plot the ground state of  $\hat{H}'$  alone as a function of  $\chi_2$  for  $N = 8$  and  $64$ . The ground state progresses from  $|N/2\rangle$  to a striped pattern as  $\chi_2$  increases. This comes about because  $\hat{H}'$  can be rewritten in a block-diagonal form with two tridiagonal blocks,

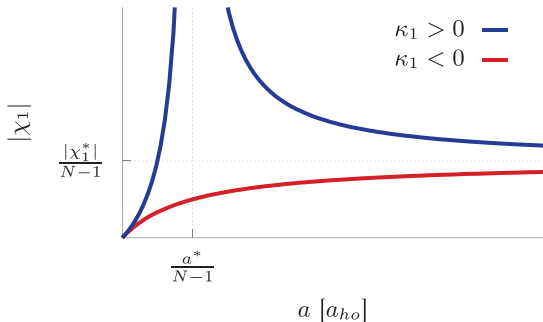


Figure 7. (Color online) Schematic plot of  $|\chi_1|$  as a function of  $a$  for both positive and negative  $\kappa_1$ . For positive  $\kappa_1$ ,  $|\chi_1|$  diverges at  $a^*/(N-1)$  and then asymptotes to  $|\chi_1^*|/(N-1)$  from above; all three regimes (Rabi-, Josephson-, and Fock-like) are present for some range of  $a$ . For negative  $\kappa_1$ ,  $|\chi_1|$  asymptotes to  $|\chi_1^*|/(N-1)$  from below, and there may or may not be Josephson- or Fock-like regimes depending on the size of  $|\chi_1^*|/(N-1)$  compared with  $N$  and  $N^{-1}$ .

where each block involves either the even-numbered or the odd-numbered Fock states. Additionally, the form of  $\hat{H}'$  invites an analogy between  $\hat{H}'$  and Eq. (32) that allows us to identify  $\chi_2 \ll N^{-1}$  as the regime in which  $-\hat{n}_l \hat{n}_r$  dominates and  $N \ll \chi_2$  as the regime in which two-body tunneling dominates.

We note that there is an additional subtlety when  $\chi_2 > 1$ . The identification of  $\chi_1$  with  $\chi$  depends on the two terms in  $\hat{H}'$  having one coefficient less than 1 and one equal to 1, which does not hold for large  $\chi_2$ . In that case, one should pull the factor of  $\chi_2$  out of  $\hat{H}'$ , and the Rabi-, Josephson-, and Fock-like regimes are defined instead by the size of the product  $\chi_1 \chi_2$ .

Given this interpretation of  $\chi_1$  and  $\chi_2$ , we can now understand the patterns in Fig. 10, where the ground state of Eq. (61) is plotted as a function of  $\chi_1$  for various values of  $\chi_2$  for  $N = 8$  and  $64$ . In the Rabi-like regime (small  $\chi_1$ ), the ground state is close to the binomial distribution of the one-body tunneling terms regardless of the size of  $\chi_2$ . In the Fock-like regime, (large  $\chi_1$ ), the ground state varies from  $|N/2\rangle$  to a wide striped pattern as  $\chi_2$  increases. The Josephson-like regime interpolates between the other two, with a narrow “neck” where the binomial and striped patterns touch. Recall that  $S$  varies like the width of these distributions (recall (Eq. (34))), so the neck corresponds to a peak in  $S$ .

With this understanding, we can now return to the trends in two-mode data presented in Figs. 5 and 6 and provide a detailed interpretation. The closer the system is to the degenerate two-mode case (i.e., larger  $L$ , smaller  $\kappa_2$ , and smaller  $\chi_2$ ), the closer the ground state will be to  $|N/2\rangle$  (as opposed to a striped state) for large  $a$ . This implies that there will generally be more squeezing with increased degeneracy. Likewise, the closer the system is to the degenerate limit, the more likely that  $S$  varies monotonically with  $a$ : because the large- $a$  state is narrower, the neck in the Josephson-like regime (and hence

the peak in  $S$ ) will be less pronounced or non-existent (upper half and rightmost plot of lower half of Figs. 5 and 6). For small values of  $a$ , increasing  $N$  tends to increase squeezing, while this is not always true for large  $a$ . This change in behavior can be understood by noting that for very large  $a$ ,  $\chi_1 = \chi_1^*/(N-1)$ . This quantity decreases as  $N$  increases, and therefore the Hamiltonian becomes increasingly dominated by the one-body tunneling terms, which have a wide distribution of Fock states in the ground state. Hence, the squeezing  $S$  is expected to *decrease* with increasing  $N$  for very large  $a$ : this is confirmed by the plots in the righthand panels of Figs. 5 and 6.

## 2. Fragmentation and Depletion

Fig. 11 shows the fragmentation parameter  $F$  as a function of  $a$  for the three double well geometries. Recall that the larger the value of  $F$ , the more fragmentation in the system. Fig. 11 shows that in general, fragmentation increases with  $a$ . An exception occurs for low  $L$  and large  $a$ , for which  $n_1$  becomes greater than  $n_0$ , and therefore the amount of squeezing drops from a maximum of 1. However, the most notable feature of these plots is that for low barriers ( $L = a_{ho}$ ), systems with larger  $N$  experience much more fragmentation than systems with smaller  $N$ , whereas the opposite is true for systems with high barriers ( $L = 3a_{ho}$ ). Equivalently, for small  $N$ , increasing the barrier height increases the amount of fragmentation, while for large  $N$ , increasing the barrier height decreases the amount of fragmentation.

We can understand these trends by examining the structure of the ground state revealed in Fig. 6. First, consider the high barrier limit ( $L = 3a_{ho}$ ). Based on the arguments above, we expect the ground state to be narrower (closer to  $|N/2\rangle$ ) for smaller  $N$ . From the analytic form of  $F$  given in Eq. (38a), we see that the terms in the sum depend on  $c_i c_{i+1}$ , i.e. the product of two adjacent  $c_i$ 's; the smaller the products, the more fragmentation there is. In general, then, we expect a narrower ground state to have more fragmentation, because it will have smaller  $c_i c_{i+1}$  products than a wider ground state (indeed, if the ground state is  $|N/2\rangle$ , all of the  $c_i c_{i+1}$  products are zero). Hence, fragmentation decreases with  $N$  at large  $a$  for  $L = 3a_{ho}$ .

For low barriers ( $L = a_{ho}$ ), the situation is different. As  $N$  increases, the ground state widens (as with  $L = 3a_{ho}$ ), but it does so by developing a striped pattern. Despite the fact that the pattern is wide for large  $N$ , the striping will cause the  $c_i c_{i+1}$  products to be small because for each pair of adjacent  $c_i$ 's, one of them will be close to zero. Hence, there will be more fragmentation for large  $N$  than for small  $N$  at large  $a$  for  $L = a_{ho}$ .

The fragmentation pattern in the intermediate barrier regime ( $L = 2a_{ho}$ ) is a crossover between the low and high barrier situations.

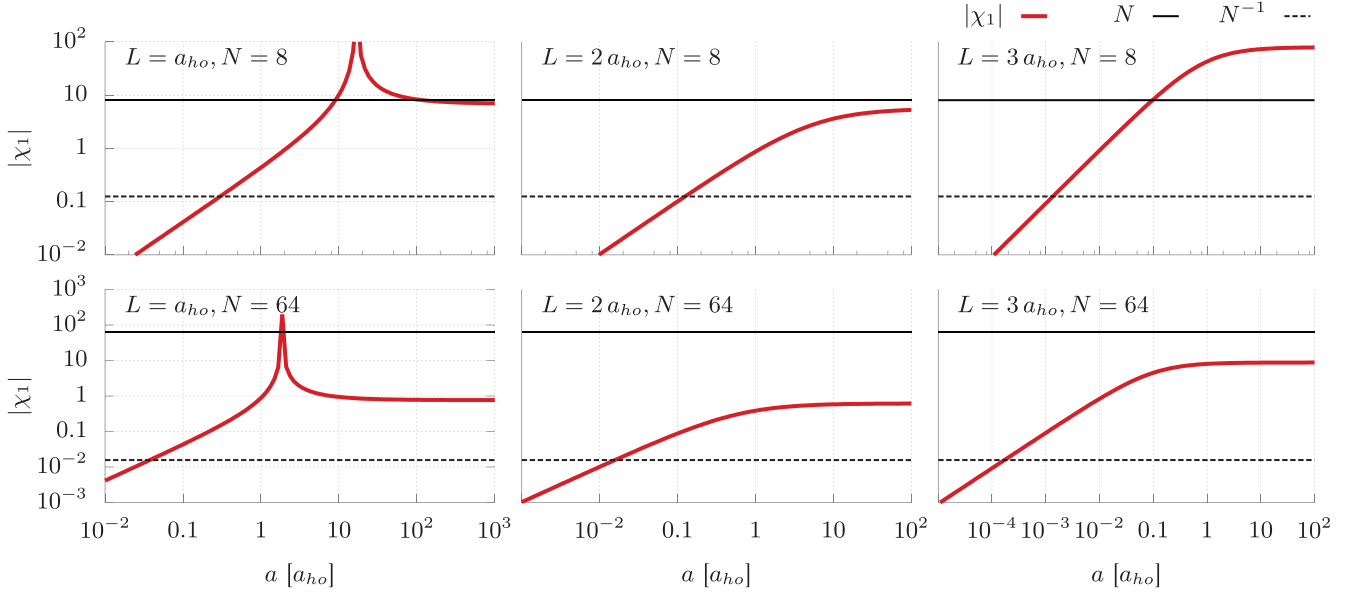


Figure 8. (Color online) The value of the parameter  $|\chi_1|$  from the full two-mode Hamiltonian (Eq. (63)) as a function of  $a$ , for  $L = a_{ho}$ ,  $2a_{ho}$ , and  $3a_{ho}$  and  $N = 8$  and  $64$ . Also indicated in each plot are the values of  $N$  (solid horizontal line) and  $N^{-1}$  (dotted horizontal line). The system is in a Rabi-like regime when  $|\chi_1|$  is below the dotted line, in a Josephson-like regime when  $|\chi_1|$  is between the two lines, and in a Fock-like regime when  $|\chi_1|$  is above the solid line. We see that while the Rabi-like regime must always be present (since  $\chi_1 = 0$  for  $a = 0$ ), the other two need not be.

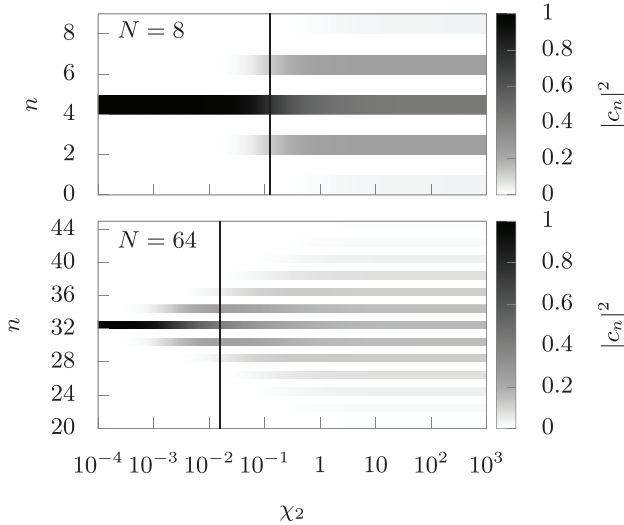


Figure 9. The components of the ground state of the Hamiltonian  $H'$ , Eq. 62, as a function of  $\chi_2$  for  $N = 8$  and  $64$ . The vertical line indicates the location of  $\chi_2 = N^{-1}$ , which forms the boundary between the values of  $\chi_2$  for which true Rabi, Josephson, and Fock regimes are found (to the left) and not found (to the right).

### 3. Summary

Previous two-mode studies, often conducted with a restricted two-mode model that is relevant only when the barrier is strong and therefore and the modes nearly de-

generate, have predicted that squeezing should monotonically increase with  $a$  and that fragmentation should monotonically increase with barrier strength. Instead, by including all possible contributions to the two-mode Hamiltonian, we find a much richer behavior, with the following characteristics:

- Squeezing is not necessarily monotonic with  $a$ , especially for weak barriers.
- For a given  $N$ , squeezing tends to increase with barrier strength.
- For a given barrier strength, squeezing tends to decrease with  $N$  for large  $a$ .
- For fixed  $a$ , fragmentation tends to increase with  $N$  for weak barriers, whereas fragmentation tends to decrease with  $N$  for strong barriers.

These trends are explained above by understanding how  $a$ ,  $N$ , and the double well geometry parameters influence the relative importance of the terms in the two-mode Hamiltonian, and therefore change the nature of the ground state. The terms in the Hamiltonian come in three types:

1. Terms that involve a single Fock state. The ground state of these terms considered alone is  $|N/2\rangle$ , which exhibits high squeezing and high fragmentation.
2. Terms that involve transitions between Fock states that involve a single atom. The ground state of

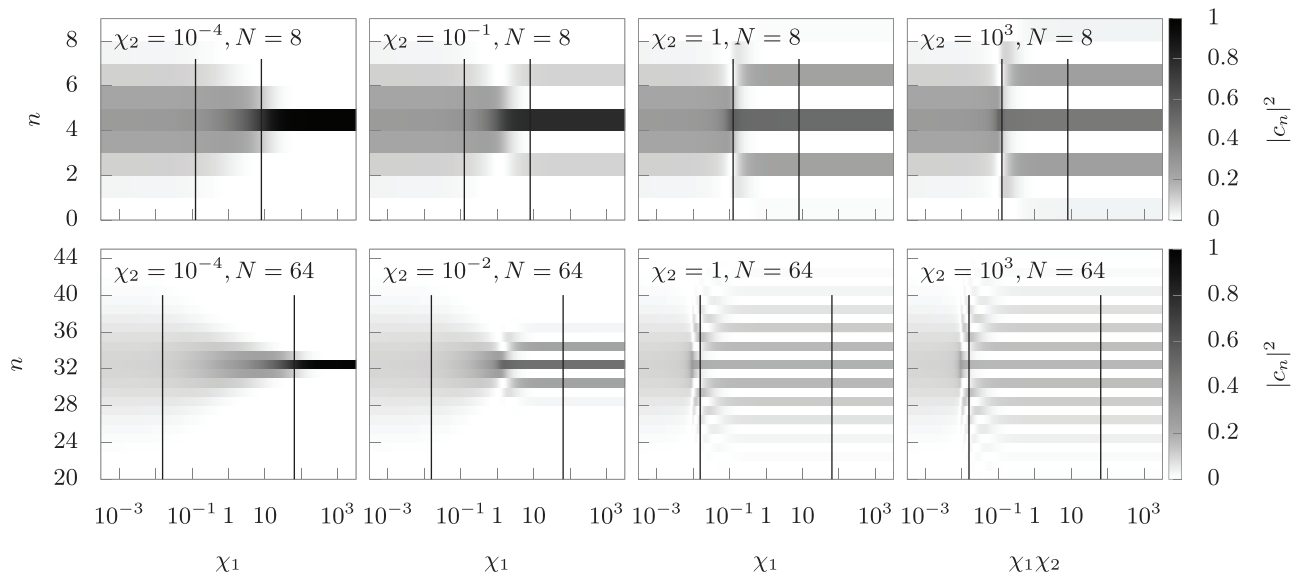


Figure 10. The components of the ground state of the full two-mode Hamiltonian Eq. (61) as a function of  $\chi_1$  ( $\chi_1\chi_2$ ), for  $N = 8$  and  $64$  and a range of  $\chi_2$  values. The vertical lines indicate the boundaries between the Rabi-, Josephson-, and Fock-like regimes, from left to right in each plot.

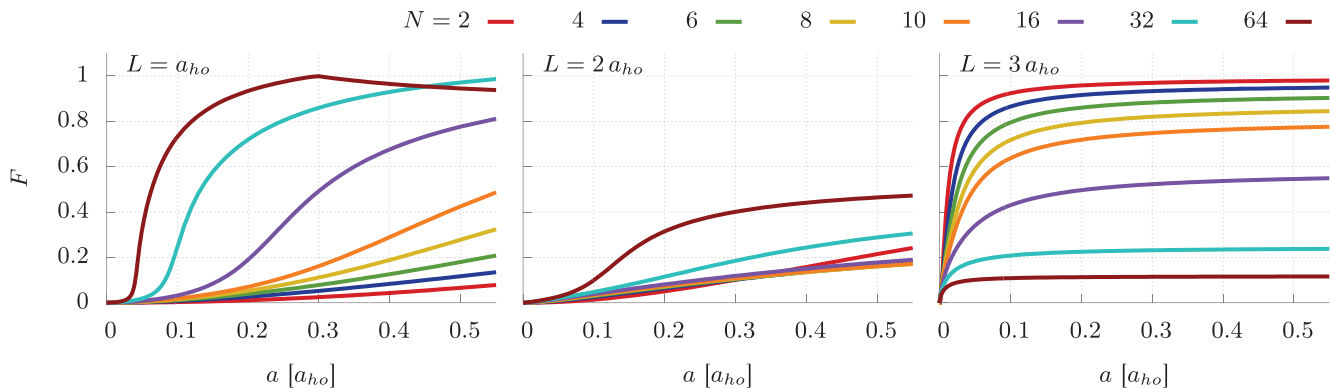


Figure 11. (Color online) Fragmentation  $F$  as a function of scattering length  $a$ , for values of particle number  $N$  between 2 and 64 for three different potentials ( $L = a_{ho}$ ,  $2 a_{ho}$ , and  $3 a_{ho}$ , from left to right) in the exact two-mode model. Because there are only two modes in this model, the depletion parameter  $D$  is necessarily zero.

these terms considered alone is a mix of states binomially distributed around  $|N/2\rangle$ , which exhibits low squeezing and low fragmentation.

- Terms that involve transitions between Fock states that involve two atoms. The ground state of these terms considered alone is a mix of *alternating* states distributed around  $|N/2\rangle$  (i.e., it includes  $|N/2\rangle$ ,  $|N/2 \pm 2\rangle$ ,  $|N/2 \pm 4\rangle$ , etc.), which exhibits high squeezing and low fragmentation.

When interactions are weak ( $|\chi_1| \ll N^{-1}$ ), type 2 terms dominate regardless of the strength of the barrier (Rabi-like regime). When interactions are strong ( $|\chi_1| \gg N$ ), the strength of the barrier matters (Fock-like regime): for low barriers ( $\chi_2 \gg N$ ), type 3 terms dominate, while

for high barriers ( $\chi_2 \ll N^{-1}$ ), type 1 terms dominate. The Josephson-like regime interpolates between these two regimes and is characterized by  $N^{-1} \ll \chi \ll N$ .

## B. Eight-mode model results

We now present the eight-mode model results for squeezing and fragmentation.

### 1. Squeezing

Fig. 12 shows the behavior of  $S$  for the eight-mode model as a function of  $a$  for  $N \leq 10$ . The squeez-

ing behavior for the low barriers ( $L = a_{ho}$  and  $2a_{ho}$ ) looks qualitatively similar to the corresponding cases in the nearly degenerate and exact two-mode models (c.f. Fig. 5). However, for  $L = 3a_{ho}$  we see qualitatively different behavior: here the squeezing has a maximum. We would like to account for this behavior, despite the fact that the eight-mode Hamiltonian cannot be analytically analyzed as easily as the two-mode Hamiltonian because of its complexity.

Since the Hilbert space for the eight-mode model is so large, it is not useful to plot the contribution to the ground state of each individual Fock state as in Fig. 6. Instead, we sum the contributions of all Fock states for which the difference in  $n_l$  and  $n_r$  is the same, regardless of which exact modes are occupied; this representation is shown in Fig. 13. By comparing Fig. 12 and Fig. 13, we see that, just as in the two-mode model, a narrower distribution corresponds to more squeezing and that the maximum in the  $L = 3a_{ho}$  squeezing data corresponds to a narrow neck in the state distribution.

It is also useful to consider the implications of the eight-mode analog to the quantity  $S_{max}$ , Eq. (35), which puts a constraint on the maximum amount of squeezing possible for the two-mode model in a given double well potential. Recall that  $S_{max}$  measures the fraction of a left or right localized state on the “wrong” side of  $z = 0$ ; the more “spillover,” the smaller  $S_{max}$ . In general, the modes that involve  $\phi_{L/R}(z)$  (with  $nlm = 210$ ) will have more spillover than the other six states, which all involve  $\phi_{l/r}(z)$  (see Eq. (41) and compare Figs. 2 and 3). This motivates us to define  $S_{max}^1$ ,

$$S_{max}^1 = \left( 1 - 2 \int_{-\infty}^0 |\phi_L(z)|^2 dz \right)^2, \quad (65)$$

as a measure of the spillover of the  $nlm = 210$  modes; this quantity is analogous to  $S_{max}$  for the  $nlm = 100$  and  $21 \pm 1$  modes. For  $L = a_{ho}$ ,  $2a_{ho}$ , and  $3a_{ho}$ ,  $S_{max} = 0.704$ ,  $0.820$ , and  $0.999$  and  $S_{max}^1 = 0.512$ ,  $0.577$ , and  $0.895$ , respectively (these values are included in Fig. 12). Both  $S_{max}$  and  $S_{max}^1$  increase with  $L$ , so there is more potential for squeezing for higher barriers. However, note that  $S_{max}^1 < S_{max}$  for each  $L$ : this implies that the 210 modes have less potential for squeezing than the other modes. Hence, by analogy with the exact two mode analysis (see discussion after Eq. (35)), we expect that a ground state will have less squeezing, other things being equal, if it is dominated by the 210 modes than if it is dominated by the others. In other words, Fock states with a given difference between  $n_l$  and  $n_r$  will contribute less to squeezing if they are dominated by the 210 modes because these modes have more spillover across  $z = 0$ .

Fig. 14 shows the fraction of particles in the eight-mode model ground state that are in the 210 modes. For a given value of  $a$ , that fraction increases with  $N$ , reaching as high as 8 percent for the largest  $N$  values. This is reasonable: in general, the repulsive interaction between the atoms drives them apart, and in an eight-mode

model, one way that the atoms can avoid each other is by occupying modes with different values of  $m$ . Hence, we expect that, for a given  $a$ , increasing the number of particles  $N$  will result in a larger fraction occupying the 210 modes. The occupation of these modes can then reduce the amount of squeezing via the spillover mechanism described above.

## 2. Fragmentation and Depletion

Fig. 15 shows the fragmentation and depletion parameters  $F$  and  $D$  (Eqs. (12)), as a function of scattering length  $a$  in the eight-mode model. The main qualitative differences between these prediction and those of the two-mode model in Fig. 11 are that the eight-mode states exhibit less fragmentation and nonzero depletion.

In the eight-mode model, there are eight natural orbitals to occupy, rather than two. The fact that there is less fragmentation and simultaneously more depletion in the eight-mode case implies that the occupation of the orbitals is spread out among more than just the first two, but also that  $n_0$  is larger relative to  $n_1$  in the eight-mode case than in the two-mode case. When there are only two modes, the only way to reduce  $n_0$  is to increase  $n_1$ . However, because there are six other natural orbitals to occupy the eight-mode model, a reduction in  $n_0$  can be compensated by an increase in any of  $n_1$  through  $n_7$ . Hence, conditions that would have led to pure fragmentation in the two-mode case lead to less fragmentation with some depletion in the eight-mode case.

## 3. Summary

Compared with the two-mode ground state, we find that the eight mode ground state

- exhibits less squeezing, especially for  $L = 3a_{ho}$ ,
- exhibits a maximum in  $S$  vs.  $a$  for  $L = 3a_{ho}$ , and
- exhibits less fragmentation and more depletion.

Physically, these effects can be understood as a consequence of the occupation of modes in the  $n = 2$  energy level in addition to the two-mode model’s  $n = 1$  modes. Since they are more delocalized across the barrier, the  $n = 2$  modes lead to greater particle fluctuations for the same value of  $N_l - N_r$  than do the  $n = 1$  modes. Hence, to the extent that they are occupied in the ground state, those  $n = 2$  modes will tend to suppress both squeezing and fragmentation in the eight-mode ground states, relative to two-mode ground states. The presence of a maximum in the squeezing parameter comes about because of a competition between this effect and the usual suppression of particle fluctuations that comes about for increased scattering length  $a$ . Finally, the presence of more than two natural orbitals in the eight-mode model

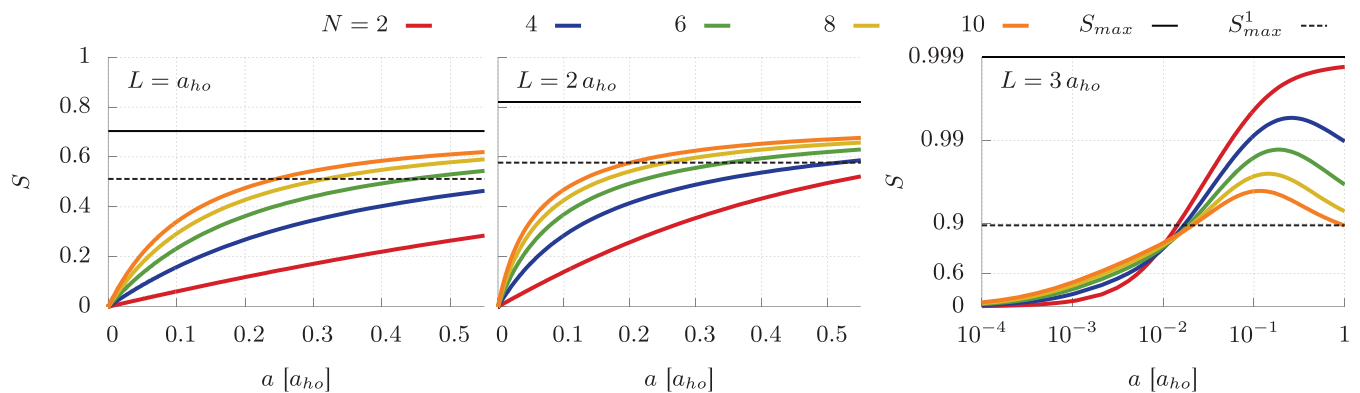


Figure 12. (Color online) Squeezing  $S$  as a function of scattering length  $a$  for values of particle number  $N$  between 2 and 10, for three different potentials ( $L = a_{ho}$ ,  $2a_{ho}$ , and  $3a_{ho}$ , from left to right) in the eight-mode model. The horizontal lines indicate the values of  $S_{max}$  and  $S_{max}^1$ .

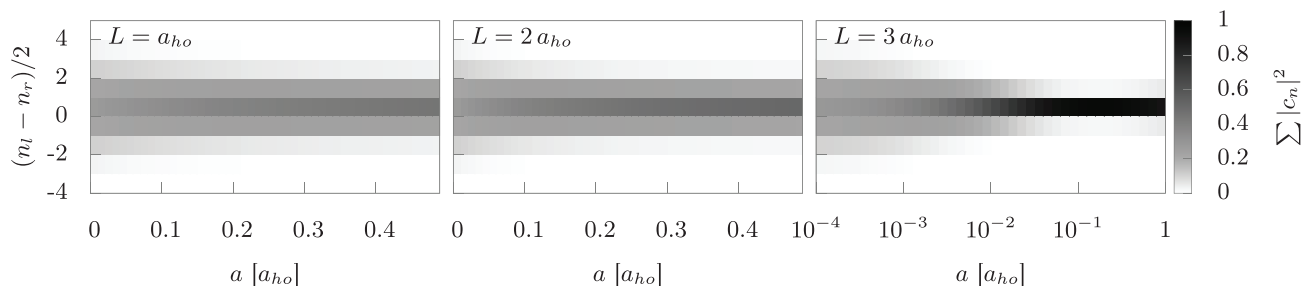


Figure 13. Representation of the ground state for the double well potential as a function of scattering length  $a$ , as computed in the eight-mode model for  $N = 8$  and various  $L$  ( $a_{ho}$ ,  $2a_{ho}$ , and  $3a_{ho}$ , from left to right). The quantity plotted in greyscale is the sum of  $|c_n|^2$  for components of the ground state with a given value for the difference between the number of particles in left and right modes,  $n_l - n_r$  ( $y$ -axis).

allows for non-zero depletion when the “extra” modes are occupied, while depletion is zero by definition in the two-mode model.

### C. Quantum Monte Carlo results

We now present the numerically exact PIGS results for squeezing and fragmentation, and compare these to the results from the truncated basis calculations within the two- and eight-mode models.

#### 1. Squeezing

Fig. 16 shows the squeezing parameter  $S$  as a function of  $a$  for the PIGS calculations, together with comparisons to the corresponding two-mode and eight-mode model results. In analogy to computations in [5], we compute a criterion of validity for the two-mode model as

$$a \ll a_c = \frac{1}{N} \sqrt{\frac{9\pi}{8L}}. \quad (66)$$

Values of  $a_c$  are indicated in Fig. 16. In general, we see that the models and the PIGS results agree well when this condition is met but deviate as  $a$  increases beyond  $a_c$ . As expected, the two-mode model shows the first deviation from the PIGS results, followed by the eight-mode model.

Whether the models tend to over- or underestimate the PIGS results for large  $a$  depends on the strength of the double well barrier (i.e., the value of  $L$ ). For strong barriers ( $L = 3a_{ho}$ ), we find less squeezing the more accurate the model (i.e., when going from two-mode to eight-mode to PIGS), whereas for weak barriers ( $L = a_{ho}$ ), we find the opposite. The intermediate-strength case ( $L = 2a_{ho}$ ) is a “crossover” between the other two cases, where the models and PIGS agree more closely.

In Sec. II B, we discussed a “conventional” explanation for why one would expect squeezing to increase with interaction strength. As  $a$  increases, the ground state changes to minimize the interparticle interaction energy, disfavoring configurations with many particles on the same side of the double well. Thus, strong repulsive interactions should suppress number fluctuations and therefore increase squeezing. However, this effect is insufficient to explain the richer squeezing behavior we see in Fig. 16

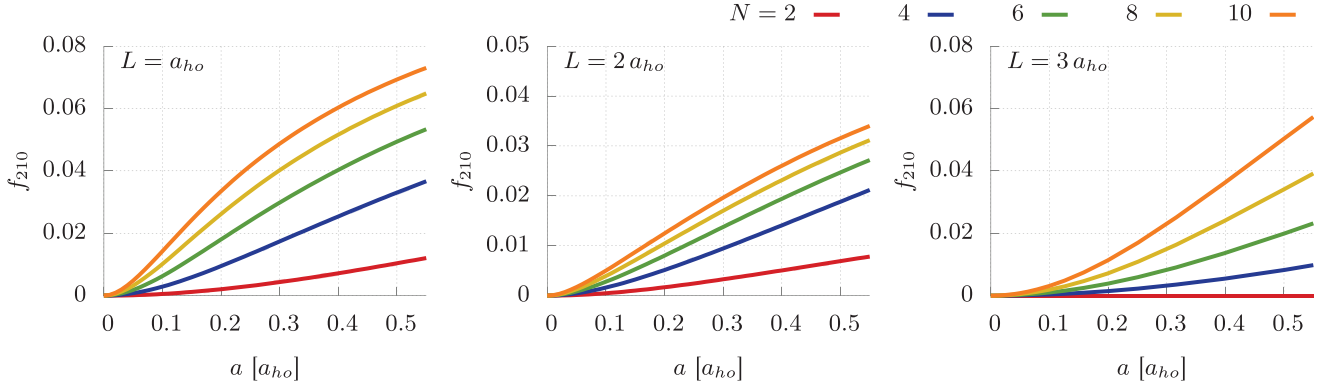


Figure 14. (Color online) Fraction  $f_{210}$  of particles in the 210 modes of the eight-mode model as a function of the scattering length  $a$ , for various particle number  $N$  between 2 and 10 and for three different potentials ( $L = a_{ho}$ ,  $2a_{ho}$ , and  $3a_{ho}$ , from left to right). The total fraction of particles in the 100 and  $21 \pm 1$  modes (not shown) is given by  $1 - f$ .

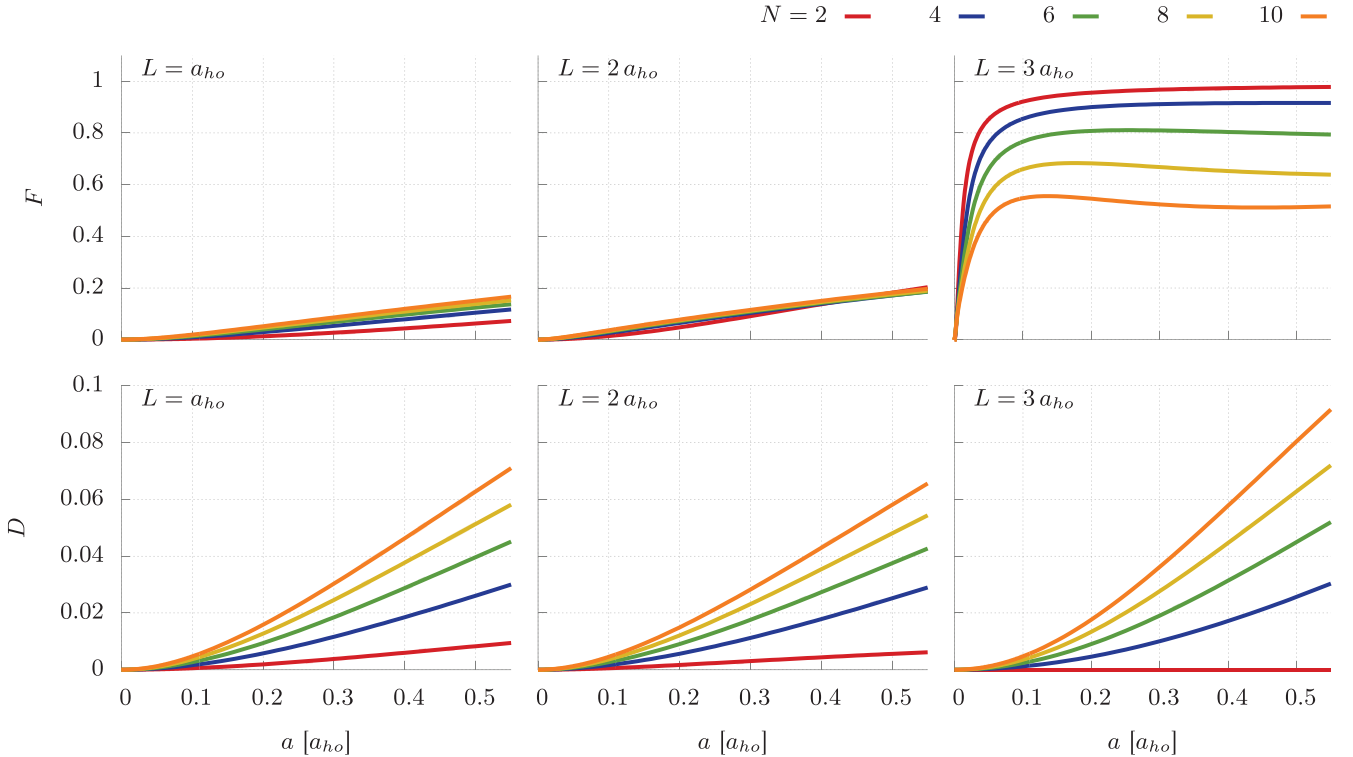


Figure 15. (Color online) Fragmentation  $F$  (top) and depletion  $D$  (bottom) as a function of scattering length  $a$  for values of particle number  $N$  between 2 and 10, for three different potentials ( $L = a_{ho}$ ,  $2a_{ho}$ , and  $3a_{ho}$ , from left to right) in the eight-mode model.

(i.e., lack of monotonicity and dependence on the double well geometry). We propose two additional mechanisms to account for this behavior.

**Delocalization Mechanism** The delocalization mechanism also involves changes in the ground state that minimize interaction energies; it is suggested by the behavior of the eight-mode ground state. As discussed in Sec. III, the eight-mode ground state contains increas-

ingly large occupation of modes in the  $n = 2$  energy level as  $a$  increases. If we treat PIGS conceptually as an “infinite-mode” model, then we would expect similar behavior in our simulations (i.e., occupation of  $n = 2$  and higher modes).

The more that a set of modes is delocalized into the “wrong” side of the double well, the less squeezing it can support. Certain modes with higher  $n$  tend to be delocalized more than the  $n = 1$  modes (the only ones present in

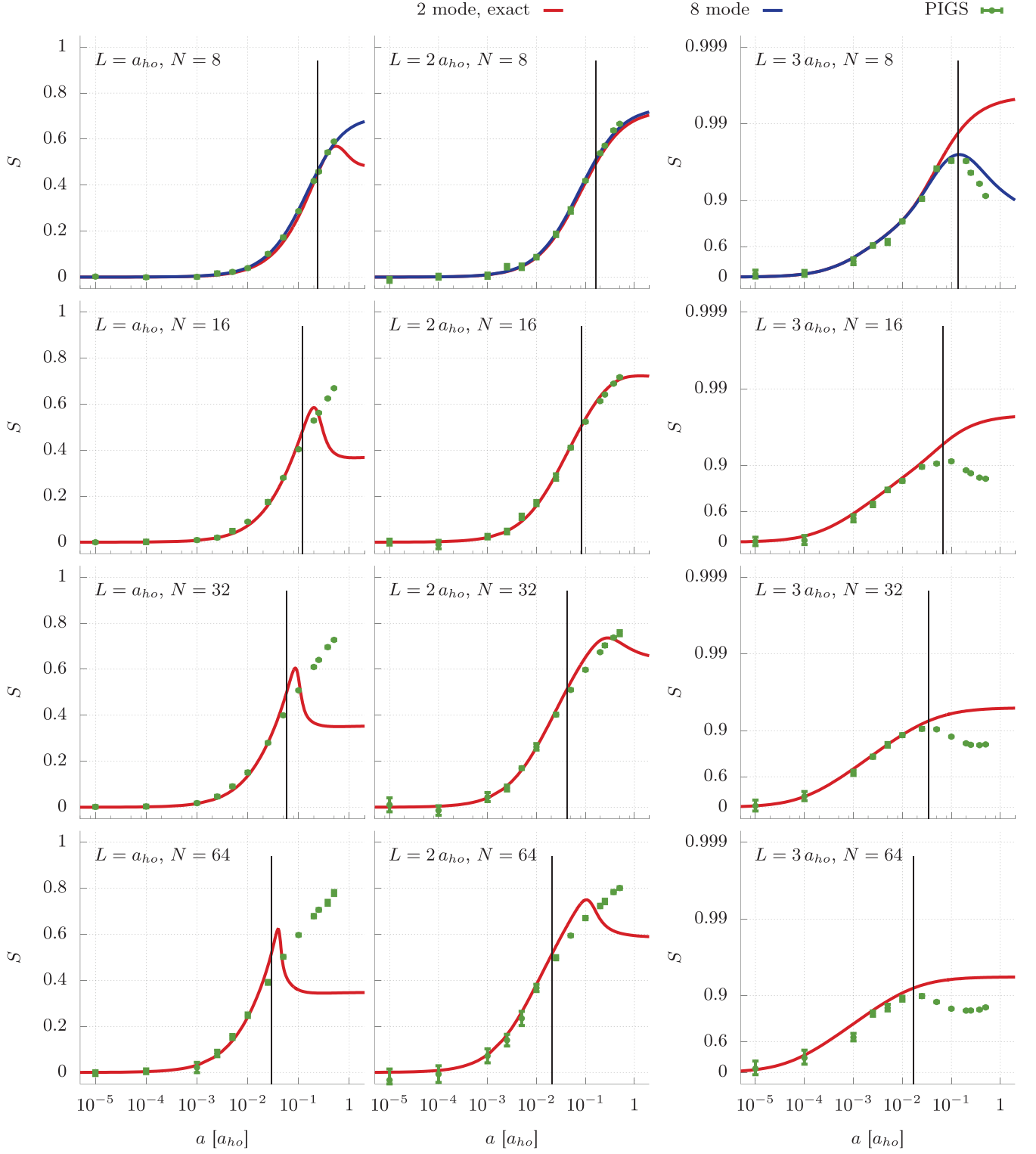


Figure 16. (Color online) Squeezing  $S$  vs. scattering length  $a$  for four different particle numbers ( $N = 8, 16, 32$ , and  $64$ , from top to bottom) and three different potentials ( $L = a_{ho}, 2a_{ho}$ , and  $3a_{ho}$ , from left to right). The plots include results from the two-mode model, the eight-mode model, and the PIGS simulations. Vertical lines indicate the value of  $a = a_c$  below which we expect the two-mode models to be valid (Eq. 66).

the two-mode model), which implies that they can support less squeezing. Hence, when strong repulsion drives particles into modes of higher  $n$ , it is driving some of them into modes that support less squeezing. Thus, this mechanism produces opposite results to the conventional mechanism, where increased  $a$  leads to increased  $S$ . Both of these mechanisms are independent of the shape of the double well (i.e., of  $L$ ).

**Tunneling Mechanism** The tunneling mechanism arises from the increase in the number of types of two-body tunneling terms due to the presence of higher modes. As described in Sec. III, two-particle tunneling terms dominate the dynamics of the system for large  $a$  and small  $L$ . In the two-mode model, these tunneling terms force the ground state to occupy even-numbered Fock states only, causing large number fluctuations and hence little squeezing. The availability of higher modes changes this situation by dramatically increasing the variety of two-particle tunneling terms in the Hamiltonian. In principle, two particles can tunnel from any two modes to any other two modes, as long as the total value of the  $z$ -component of their angular momentum is conserved. Hence, the alternating-Fock-state restriction is lifted, and the ground state can have contributions from Fock states with any value of  $|n_l - n_r|$ . This leads to a reduction in the occupation of modes with large values of  $|n_l - n_r|$ , and hence squeezing will be greater than predicted by the two-mode model. Again treating the PIGS simulations as “infinite-mode” implies that this effect will be more pronounced in the Quantum Monte Carlo than in the eight-mode model results.

This tunneling mechanism varies in importance depending on the value of  $L$ . For small  $L$ , it operates as described above. However, for large  $L$ , tunneling between the wells is highly suppressed for all modes. In the two-mode case, this drives the ground state towards  $|N/2\rangle$ , an equal splitting of particles. The presence of higher modes has little effect on this distribution, again because all tunneling between the wells is suppressed. Therefore, the amount of squeezing is not be affected for large  $L$ .

**Interaction of Mechanisms** In summary, the delocalization mechanism tends to reduce the amount of squeezing compared with the two-mode model and is relevant for any  $L$ , while the tunneling mechanism tends to increase squeezing compared with the two-mode model and is only important for small  $L$ . The combination of these effects explains the patterns seen in Fig. 16. For small  $L$ , the tunneling mechanism dominates, and there is more squeezing than predicted by the two-mode model. For large  $L$ , the delocalization mechanism dominates, and there is less squeezing than predicted by the two-mode model.

A marked feature of the Quantum Monte Carlo results is the lack of monotonicity in the  $L = 3a_{ho}$  PIGS data (righthand column of Fig. 16). This effect is likely due to an interplay between the the “conventional” mechanism,

which increases squeezing, and the delocalization mechanism, which suppresses squeezing, as the interactions become more repulsive.

## 2. Validity of the Two-Body Interaction Approximation

Fig. 17 shows the PIGS squeezing data of Fig. 16, plotted now as a function of  $Na$  for each value of  $L$ . The most striking feature of this plot is that the data for the various values of  $N$  overlap each other (with the exception of the  $N = 8$  data for the strongest barrier ( $L = 3a_{ho}$ ), which shows slightly more squeezing for large  $Na$  than the other values of  $N$ ). Thus we have found that to a good approximation,  $S$  is a function of the product  $Na$  for the potentials and ranges of  $N$  and  $a$  presented here.

One can show that the only situation in which the interaction Hamiltonian depends on the product  $Na$  is when only two-body interactions are relevant to the physics. If higher-body interactions play a significant role, then the interaction Hamiltonian depends in a more complicated manner on  $N$  and  $a$  [74]. Thus, Fig. 17 indicates that only two-body interactions are relevant for the squeezing of the double well system in the parameter regime presented here. This is a non-trivial observation because the form of the hard sphere propagator used in the PIGS simulations, Eq. (56), can take into account interactions among an arbitrary number of particles. Evidently, the two-body approximation that enters into the two- and eight-mode models is not responsible for any discrepancies between the results of the models and the PIGS simulations.

Additionally, the universality of the scaling of squeezing with  $Na$  across all of our data suggests that we can extrapolate our squeezing results to systems with larger values of  $N$  than simulated here, with correspondingly lower values of  $a$ . It also suggests that to compute additional results for larger  $N$ , one could simulate systems with the same  $N$  but larger  $a$ . This observation therefore mitigates the system size limitation inherent in our PIGS calculations for as long as this universality continues to hold.

## 3. Fragmentation and Depletion

We now discuss the fragmentation and depletion results. Fig. 18 shows the fragmentation parameter  $F$  as a function of  $a$  for PIGS simulations with the same ranges of  $N$ ,  $L$ , and  $\alpha$  as before, together with comparison to the equivalent two- and eight-mode models. For weak barriers ( $L = 2a_{ho}$  and  $3a_{ho}$ ), there is a relatively modest amount of fragmentation at large  $a$ . For  $L = 3a_{ho}$  and small  $N$ , there is a relatively large amount of fragmentation for large  $a$ . The amount of fragmentation decreases with increasing  $N$ . Additionally, as for squeezing, we find that the amount of fragmentation present does not vary monotonically with  $a$ . Fig. 19 shows the depletion

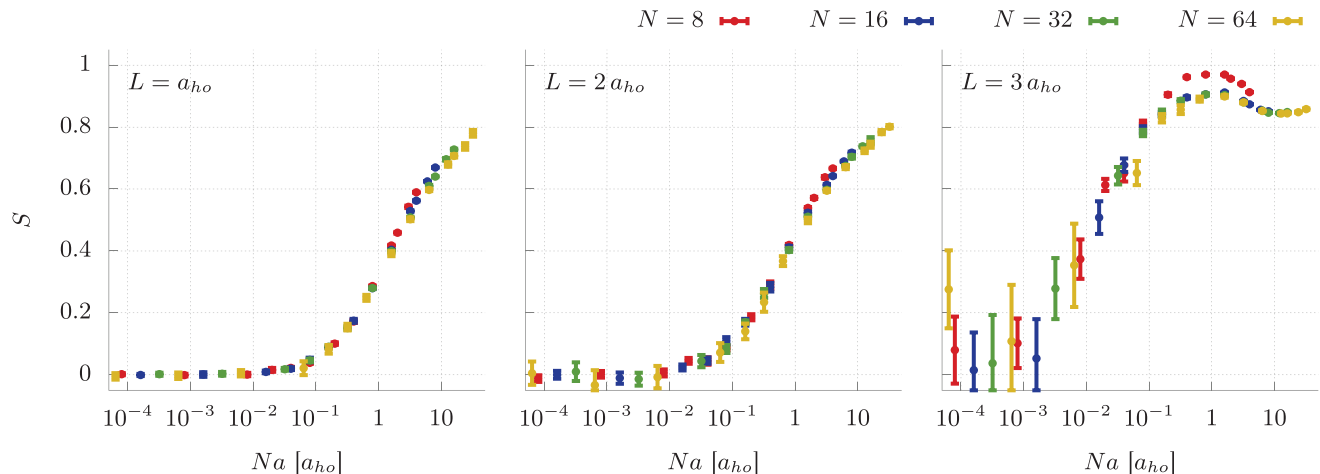


Figure 17. (Color online) Universal scaling of the Quantum Monte Carlo (PIGS) results for the squeezing parameter  $S$  vs.  $Na$  (the product of the number of atoms and the scattering length) for three different potentials ( $L = a_{ho}$ ,  $2a_{ho}$ , and  $3a_{ho}$ , from left to right).

parameter  $D$  as a function of  $a$  (c.f. Fig. 18). We see a modest increase in depletion, of comparable size in all parameter regimes, for large values of  $a$ .

In both Fig. 19 and Fig. 18, the vertical lines indicate the values of  $a$  below which the two-mode model is expected to be sufficient to describe the physics of the system ( $a \leq a_c$ ). As was seen for squeezing, the truncated basis models and PIGS results agree well when  $a < a_c$ , but deviate as  $a$  increases beyond this value. The deviation takes the form of less fragmentation than predicted in the  $n$ -mode models and less depletion than in the eight-mode model. We also see approximately the same amount of depletion in the system for all  $N$  and  $L$  values.

The reduction in fragmentation can be accounted for by the mechanisms described in Sec. VC1. Fragmentation in the double well system increases when the wells are more “isolated”, i.e., when it is unlikely for a particle to tunnel from one well to the other. Thus potentials with larger  $L$  experience more fragmentation. The delocalization mechanism entails the occupation of modes with higher values of  $n$ , some of which have more spillover into the “wrong” side of the double well than the  $n = 1$  modes. Hence, the occupation of these modes will lessen the isolation of the wells by putting atoms in states that span both sides of the double well barrier and hence reduce fragmentation.

Additionally, we found that the fragmentation  $F$  is large in the two-mode case when alternating Fock states are occupied. This is only possible for small  $L$ . The tunneling mechanism involves the presence of many two-body tunneling terms due to the addition of modes beyond  $n = 1$ , and these terms prevent the system from forming a state that occupies alternating Fock states. Hence, this effect causes a dramatic reduction in fragmentation compared with the two-mode model.

Finally, we comment on the degree of depletion seen in the PIGS data. From the analysis of Bogoliubov [59], we know that depletion begins to become significant in a homogeneous BEC when  $an^{1/3}$  approaches 1 (where  $n$  is the particle density). Fig. 20 plots  $an^{1/3}$  as a function of the scattering length for the PIGS data, where we have approximated  $n$  as the maximum value of the quantity  $N\rho_x(x)\rho_y(y)\rho_z(z)$ , with  $\rho_i$  the single-body density in the  $i$  direction. We choose the maximum value because depletion will be dominated by the parts of the BEC where the density is greatest. We see that  $an^{1/3}$  is very close to 1 for large values of  $a$  and is essentially independent of  $N$  and  $L$ , consistent with the depletion results shown in Fig. 19.

## VI. CONCLUSION

We have presented a detailed analytical and numerical study of the squeezing and fragmentation exhibited by the ground state of an ultracold, bosonic atomic gas in a three-dimensional double well trap for a variety of particle number, interaction strengths, and double well trap geometries, using exact ground state calculations with Quantum Monte Carlo methods and comparing to truncated basis models with two and eight modes only. In making these comparison, we have extended the previous two-mode analyses with analysis of the exact two-mode Hamiltonian and investigated for the first time the squeezing and fragmentation phenomena of a recently-proposed eight-mode model. Using numerically exact Quantum Monte Carlo methods to simulate the system led to a number of interesting and surprising discoveries about these well-known systems, most notably the fact that squeezing and fragmentation show non-monotonic behavior with interaction strength.

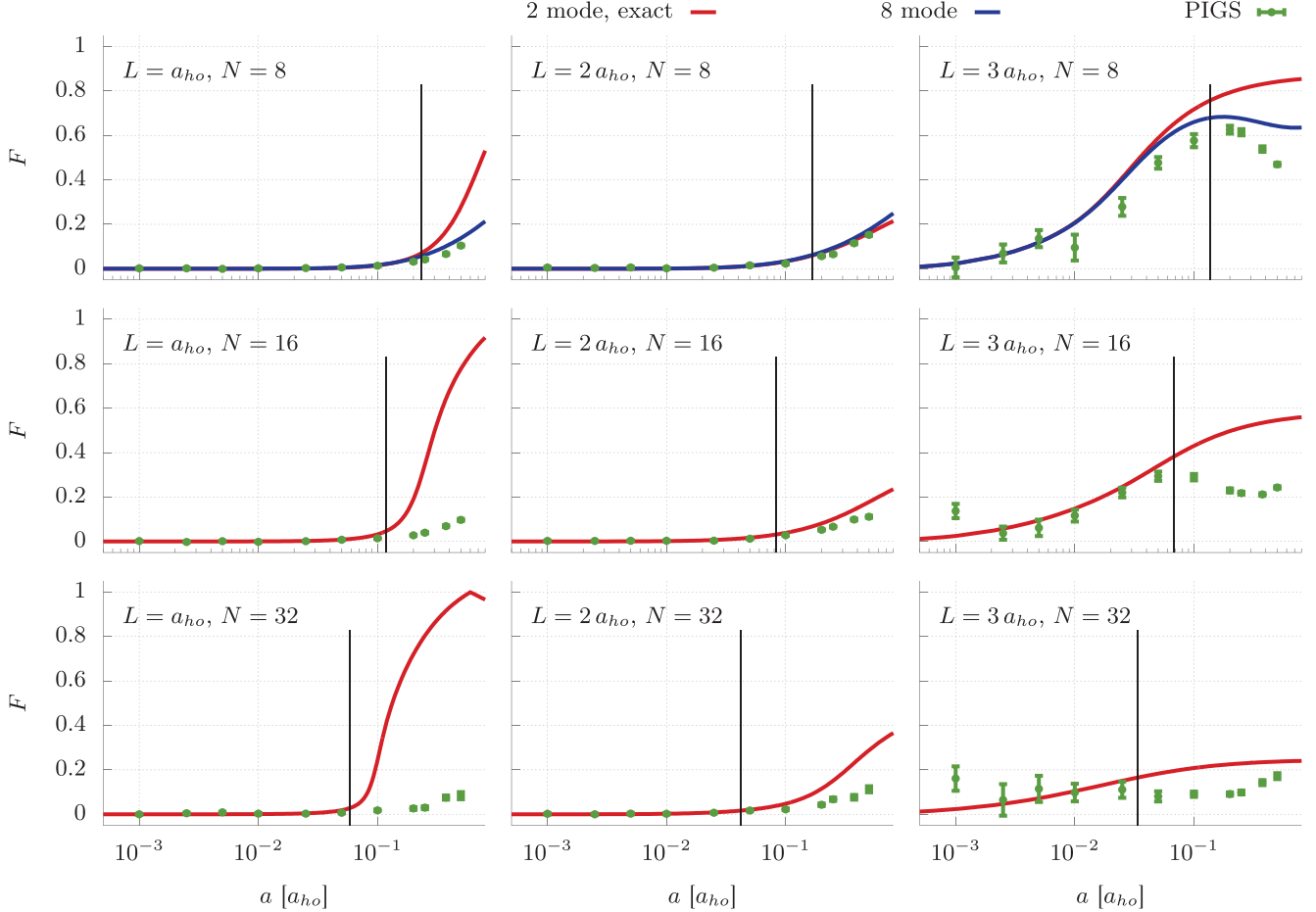


Figure 18. (Color online) Quantum Monte Carlo results for the fragmentation parameter  $F$  vs. scattering length  $a$ , for four different particle numbers ( $N = 8, 16, 32$ , and  $64$ , from top to bottom) and three different potentials ( $L = a_{ho}, 2 a_{ho}$ , and  $3 a_{ho}$ , from left to right). The plots include results from the exact two-mode model, the eight-mode model, and the PIGS simulations. Vertical lines indicate the values of  $a = a_c$  below which we expect the two-mode model to be valid (Eq. 66).

The quantitative understanding gained from this study allows for a more sophisticated qualitative picture of the way in which squeezing and fragmentation come about in a double well system than was previously possible. Recall that the suppression of number fluctuations corresponds to increased squeezing and the suppression of tunneling corresponds to increased fragmentation. Both the old and the new qualitative pictures start the same way:

The ground state of the noninteracting double well is a product of the single-body ground state of each particle, and these single-body states each occupy both wells equally. Hence, if one were to measure the number of atoms in the left well minus the number in the right well, one could get any value from  $N$  to  $-N$ . Therefore, number fluctuations are large and squeezing is small. An equivalent way to think of this situation is that the structure of the noninteracting ground state is such that tunneling is strong, and therefore fragmen-

tation is small. In fact, both  $S$  and  $F$  are defined to be 0 in the noninteracting case.

In the old picture, the introduction of repulsive interacting proceeds like this:

The introduction of repulsive interactions causes the system to minimize its interacting energy by suppressing configurations in which many particles are in one well and few are on the other. This reduces number fluctuations and increases squeezing. Additionally, moving towards a configuration in which  $N/2$  particles are locked into each side of the double well suppresses tunneling and increases fragmentation. These effects increase with increasing interacting strength.

However, in the new picture, the introduction of repulsive interactions proceeds as follows:

The introduction of repulsive interactions

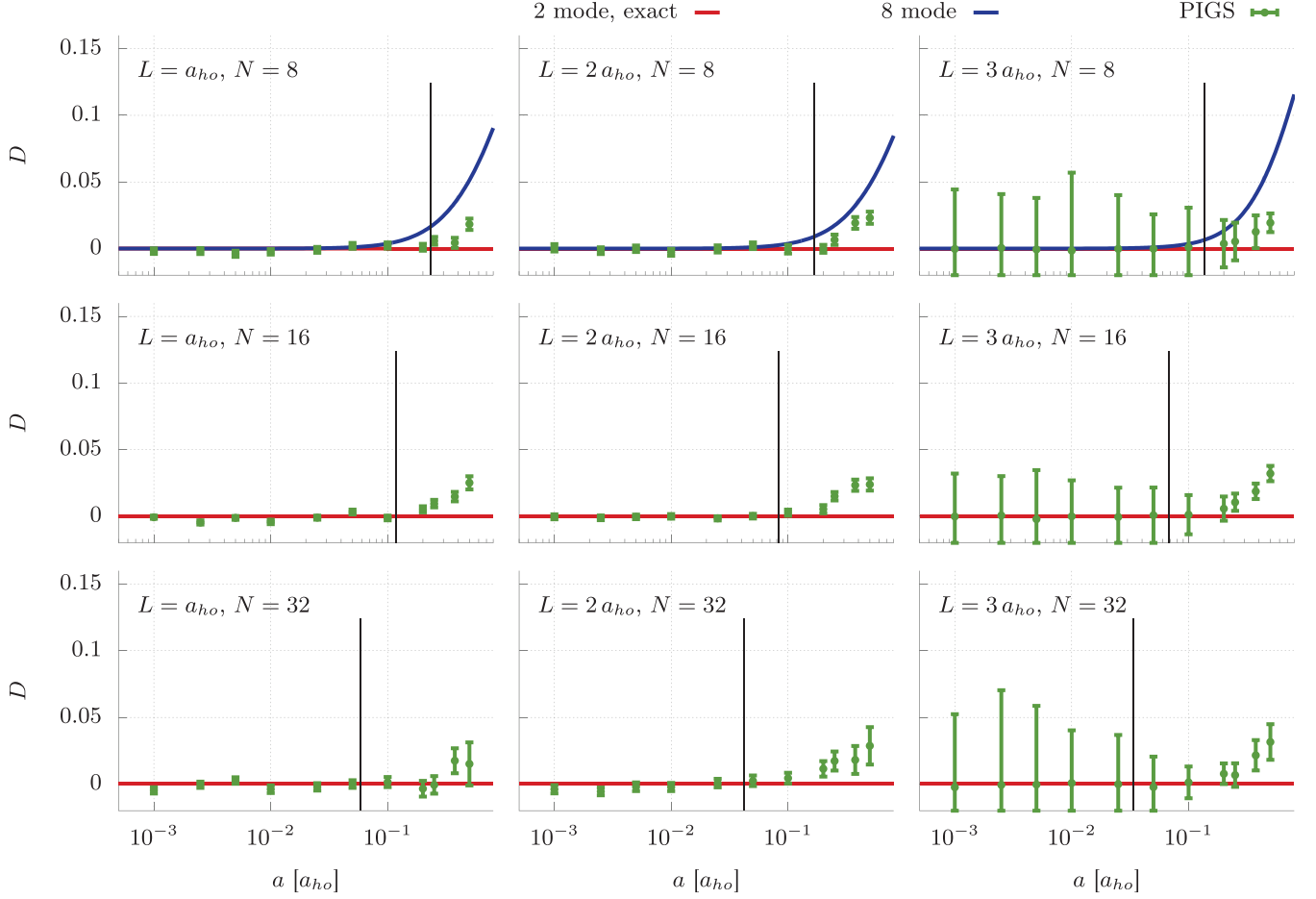


Figure 19. (Color online) Quantum Monte Carlo results for the depletion parameter  $D$  vs. scattering length  $a$ , for four different particle numbers ( $N = 8, 16, 32$ , and  $64$ , from top to bottom) and three different potentials ( $L = a_{ho}, 2 a_{ho}$ , and  $3 a_{ho}$ , from left to right). The plots include results from the exact two-mode model, the eight-mode model, and the PIGS simulations. Vertical lines indicate the values of  $a = a_c$  below which we expect the two-mode model to be valid (Eq. eq:PIGSbreakdown).

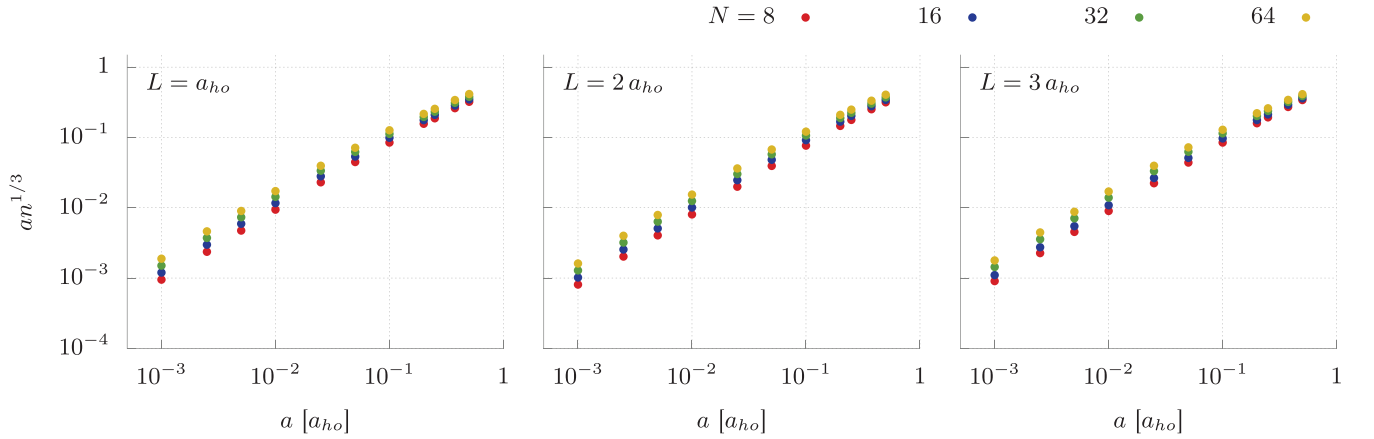


Figure 20. (Color online) Quantum Monte Carlo results for the dimensionless quantity  $an^{1/3}$  vs. scattering length  $a$ , for four different particle numbers ( $N = 8, 16, 32$ , and  $64$ ) and three different potentials ( $L = a_{ho}, 2 a_{ho}$ , and  $3 a_{ho}$ , from left to right). The condition  $an^{1/3} \ll 1$  specifies the condition under which depletion should be negligible in a homogeneous BEC. Note that the relationship between  $an^{1/3}$  and  $a$  is essentially unaffected by changes in  $N$  or  $L$ .

causes the system to minimize its interacting energy in several ways. One way is to suppress configurations in which many particles are in one well and few are on the other. This increases squeezing and fragmentation as in the old picture. However, the system can also reduce its interaction energy by promoting atoms to modes in higher energy levels ( $n > 1$ ). One can approximate these modes as each being localized in one of the two wells, although they will extend into the “wrong” well based on the strength of the double well barrier. There are some modes in each energy band  $n > 1$  that extend into the wrong well much further than the  $n = 1$  modes. Hence, a ground state dominated by modes with larger values of  $n$  naturally have larger number fluctuations and tunneling than ground states dominated by  $n = 1$  modes, and therefore they exhibit less squeezing and fragmentation. These two effects compete with each other to determine the overall amount of squeezing and fragmentation, which is not monotonic in many cases.

Thus, for sufficiently large values of  $a$ , one cannot appeal to either mean-field or multi-mode modes to correctly predict the amount of squeezing and fragmentation exhibited by the system. Instead, one must deploy the full machinery of a numerically-exact method like Quantum Monte Carlo, which allows for full three-dimensional calculations without restriction to a truncated basis set representation. These results show that for a given double well potential, the amount of squeezing is a function solely of the product  $Na$ .

Finally, we would like to revisit one of the main motivations of this work discussed in the introduction, namely the application of squeezed states to reduce the measure-

ment uncertainty of atom interferometers. In general, the more squeezed the states used in the interferometers, the smaller the uncertainty. One way to generate a highly squeezed state is to use a Feshbach resonance to tune the interaction strength of the atoms in a BEC, thereby changing the amount of squeezing exhibited by the system. However, what interaction strength is the one that *maximizes* squeezing? In the context of the old qualitative picture, the answer is simple: stronger repulsive interactions mean more squeezing, so one should tune  $a$  to as large a value as one can. However, we have shown that the real picture is far more complicated: squeezing does not increase monotonically with interaction strength in many situations, and there is often some optimal value of  $a$  that maximizes squeezing that one cannot predict through the use of  $n$ -mode models but must instead calculate from the full Hamiltonian, using an exact but computationally expensive method like PIGS. With the increasingly rapid advances of experimental methods for the study of Bose-Einstein condensates, we look forward to laboratory confirmation of the results of this study in the near future.

## VII. ACKNOWLEDGEMENTS

This research was supported by the National Science Foundation and by the UC Lab Fees Research Program under a grant to the University of California, Berkeley and Lawrence Livermore National Laboratory. J.L.D. acknowledges work performed under the auspices of the U.S. Department of Energy by Lawrence Livermore National Laboratory under Contract No. DE-AC52-07NA27344. K.B.W and J.C.C. also thank the Kavli Institute for Theoretical Physics for their hospitality and for supporting this research in part by the National Science Foundation Grant No. PHY11-25915.

- 
- [1] K. B. Davis, M.-O. Mewes, M. R. Andrews, N. J. van Druten, D. S. Durfee, D. M. Kurn, and W. Ketterle, *Phys. Rev. Lett.* **75**, 3969 (1995).
  - [2] M. H. Anderson, J. R. Ensher, M. R. Matthews, C. E. Wieman, and E. A. Cornell, *Science* **269**, 198 (1995).
  - [3] K. W. Mahmud, J. N. Kutz, and W. P. Reinhardt, *Phys. Rev. A* **66**, 063607 (2002).
  - [4] K. W. Mahmud, H. Perry, and W. P. Reinhardt, *Phys. Rev. A* **71**, 023615 (2005).
  - [5] G. J. Milburn, J. Corney, E. M. Wright, and D. F. Walls, *Phys. Rev. A* **55**, 4318 (1997).
  - [6] J. Javanainen and M. Y. Ivanov, *Phys. Rev. A* **60**, 2351 (1999).
  - [7] C. Bodet, J. Estève, M. K. Oberthaler, and T. Gasenzer, *Phys. Rev. A* **81**, 063605 (2010).
  - [8] R. W. Spekkens and J. E. Sipe, *Phys. Rev. A* **59**, 3868 (1999).
  - [9] E. J. Mueller, T.-L. Ho, M. Ueda, and G. Baym, *Phys. Rev. A* **74**, 033612 (2006).
  - [10] K. Sakmann, A. I. Streltsov, O. E. Alon, and L. S. Cederbaum, *Phys. Rev. A* **84**, 053622 (2011).
  - [11] D. Ananikian and T. Bergeman, *Phys. Rev. A* **73**, 013604 (2006).
  - [12] X. Jia, W. Li, and J. Q. Liang, *Phys. Rev. A* **78**, 023613 (2008).
  - [13] D.-S. Lühmann, O. Jürgensen, and K. Sengstock, *New J. Phys.* **14**, 033021 (2012).
  - [14] I. Zapata, F. Sols, and A. J. Leggett, *Phys. Rev. A* **57**, R28 (1998).
  - [15] F. Meier and W. Zwerger, *Phys. Rev. A* **64**, 033610 (2001).
  - [16] J. Gillet, M. A. Garcia-March, T. Busch, and F. Sols, *Phys. Rev. A* **89**, 023614 (2014).
  - [17] M. A. García-March, D. R. Dounas-Frazer, and L. D. Carr, *Phys. Rev. A* **83**, 043612 (2011).

- [18] A. I. Streltsov, O. E. Alon, and L. S. Cederbaum, *Phys. Rev. A* **73**, 063626 (2006).
- [19] D. Masiello, S. B. McKagan, and W. P. Reinhardt, *Phys. Rev. A* **72**, 063624 (2005).
- [20] S. Zöllner, H.-D. Meyer, and P. Schmelcher, *Phys. Rev. A* **74**, 053612 (2006).
- [21] K. Sakmann, A. I. Streltsov, O. E. Alon, and L. S. Cederbaum, *Phys. Rev. A* **78**, 023615 (2008).
- [22] H. Feshbach, *Ann. Phys.* **5**, 357 (1958).
- [23] D. J. Wineland, J. J. Bollinger, W. M. Itano, F. L. Moore, and D. J. Heinzen, *Phys. Rev. A* **46**, R6797 (1992).
- [24] D. J. Wineland, J. J. Bollinger, W. M. Itano, and D. J. Heinzen, *Phys. Rev. A* **50**, 67 (1994).
- [25] J. J. Bollinger, W. M. Itano, D. J. Wineland, and D. J. Heinzen, *Phys. Rev. A* **54**, R4649 (1996).
- [26] S. F. Huelga, C. Macchiavello, T. Pellizzari, A. K. Ekert, M. B. Plenio, and J. I. Cirac, *Phys. Rev. Lett.* **79**, 3865 (1997).
- [27] J. A. Dunningham, K. Burnett, and S. M. Barnett, *Phys. Rev. Lett.* **89**, 150401 (2002).
- [28] J. A. Dunningham and K. Burnett, *Phys. Rev. A* **70**, 033601 (2004).
- [29] C. Orzel, A. K. Tuchman, M. L. Fenselau, M. Yasuda, and M. A. Kasevich, *Science* **291**, 2386 (2001).
- [30] C.-S. Chuu, F. Schreck, T. P. Meyrath, J. L. Hanssen, G. N. Price, and M. G. Raizen, *Phys. Rev. Lett.* **95**, 260403 (2005).
- [31] G.-B. Jo, Y. Shin, S. Will, T. A. Pasquini, M. Saba, W. Ketterle, D. E. Pritchard, M. Vengalattore, and M. Prentiss, *Phys. Rev. Lett.* **98**, 030407 (2007).
- [32] W. Li, A. K. Tuchman, H.-C. Chien, and M. A. Kasevich, *Phys. Rev. Lett.* **98**, 040402 (2007).
- [33] J. Esteve, C. Gross, A. Weller, S. Giovanazzi, and M. K. Oberthaler, *Nature* **455**, 1216 (2008).
- [34] J. Appel, P. J. Windpassinger, D. Oblak, U. B. Hoff, N. Kjærgaard, and E. S. Polzik, *Proc. Natl. Acad. Sci. USA* **106**, 10960 (2009).
- [35] C. Gross, T. Zibold, E. Nicklas, J. Estève, and M. K. Oberthaler, *Nature* **464**, 1165 (2010).
- [36] M. Kitagawa and M. Ueda, *Phys. Rev. A* **47**, 5138 (1993).
- [37] A. Sorensen, L.-M. Duan, J. I. Cirac, and P. Zoller, *Nature* **409**, 63 (2001).
- [38] F. Cattani, C. Gross, M. K. Oberthaler, and J. Ruostekoski, *New J. Phys.* **15**, 063035 (2013).
- [39] Sinatra, Alice, Castin, Yvan, and Witkowska, Emilia, *EPL* **102**, 40001 (2013).
- [40] C. Gross, J. Estève, M. K. Oberthaler, A. D. Martin, and J. Ruostekoski, *Phys. Rev. A* **84**, 011609 (2011).
- [41] I. D. Leroux, M. H. Schleier-Smith, and V. Vuletić, *Phys. Rev. Lett.* **104**, 250801 (2010).
- [42] Z. Chen, J. G. Bohnet, S. R. Sankar, J. Dai, and J. K. Thompson, *Phys. Rev. Lett.* **106**, 133601 (2011).
- [43] M. F. Riedel, P. Bohi, Y. Li, T. W. Hansch, A. Sinatra, and P. Treutlein, *Nature* **464**, 1170 (2010).
- [44] P. Nozières and D. Saint James, *J. Phys. France* **43**, 1133 (1982).
- [45] K. Xu, Y. Liu, D. E. Miller, J. K. Chin, W. Setiawan, and W. Ketterle, *Phys. Rev. Lett.* **96**, 180405 (2006).
- [46] A. E. Leanhardt, A. P. Chikkatur, D. Kielpinski, Y. Shin, T. L. Gustavson, W. Ketterle, and D. E. Pritchard, *Phys. Rev. Lett.* **89**, 040401 (2002).
- [47] A. I. Streltsov, L. S. Cederbaum, and N. Moiseyev, *Phys. Rev. A* **70**, 053607 (2004).
- [48] A. D. Jackson, G. M. Kavoulakis, and M. Magiropoulos, *Phys. Rev. A* **78**, 063623 (2008).
- [49] A. Sarsa, K. E. Schmidt, and W. R. Magro, *J. Chem. Phys.* **113**, 1366 (2000).
- [50] S. Moroni and M. Boninsegni, *J. Low Temp. Phys.* **136**, 129 (2004).
- [51] J. E. Cuervo, P.-N. Roy, and M. Boninsegni, *J. Chem. Phys.* **122**, 114504 (2005).
- [52] W. Krauth, *Phys. Rev. Lett.* **77**, 3695 (1996).
- [53] Y. Shin, M. Saba, T. A. Pasquini, W. Ketterle, D. E. Pritchard, and A. E. Leanhardt, *Phys. Rev. Lett.* **92**, 050405 (2004).
- [54] S. E. Pollack, D. Dries, M. Junker, Y. P. Chen, T. A. Corcovilos, and R. G. Hulet, *Phys. Rev. Lett.* **102**, 090402 (2009).
- [55] O. Penrose and L. Onsager, *Phys. Rev.* **104**, 576 (1956).
- [56] A. J. Leggett, *Rev. Mod. Phys.* **73**, 307 (2001).
- [57] P.-O. Löwdin, *Phys. Rev.* **97**, 1474 (1955).
- [58] T. D. Lee, K. Huang, and C. N. Yang, *Phys. Rev.* **106**, 1135 (1957).
- [59] N. Bogoliubov, *Изв. АН СССР, Сер. физ. (Bull. Acad. Sci. USSR, Phys.)* **11**, 77 (1947).
- [60] E. Fermi, *Ricerca Sci.* **7**, 13 (1936).
- [61] G. Breit, *Phys. Rev.* **71**, 215 (1947).
- [62] C. P. Friedman and E. F. Taylor, *Am. J. Phys.* **39**, 1073 (1971).
- [63] N. Metropolis, A. W. Rosenbluth, M. N. Rosenbluth, A. H. Teller, and E. Teller, *J. Chem. Phys.* **21**, 1087 (1953).
- [64] S. A. Chin and C. R. Chen, *J. Chem. Phys.* **117**, 1409 (2002).
- [65] J. A. Barker, *J. Chem. Phys.* **70**, 2914 (1979).
- [66] G. Jacucci and E. Omerti, *J. Chem. Phys.* **79**, 3051 (1983).
- [67] J. Cao and B. J. Berne, *J. Chem. Phys.* **97**, 2382 (1992).
- [68] S. Y. Larsen, *J. Chem. Phys.* **48**, 1701 (1968).
- [69] P. Lévy, *Compositio Math.* **7**, 283 (1940).
- [70] D. M. Ceperley, *Rev. Mod. Phys.* **67**, 279 (1995).
- [71] W. Krauth, *Statistical Mechanics: Algorithms and Computations* (Oxford University Press, 2006).
- [72] R. H. Swendsen and J.-S. Wang, *Phys. Rev. Lett.* **57**, 2607 (1986).
- [73] F. Wang and D. P. Landau, *Phys. Rev. Lett.* **86**, 2050 (2001).
- [74] J. L. DuBois and H. R. Glyde, *Phys. Rev. A* **63**, 023602 (2001).